Materials Today Chemistry 55 (2026) 103801

Contents lists available at ScienceDirect

Materials Today Chemistry

journal homepage: www.journals.elsevier.com/materials-today-chemistry/

# From wood pulp fibers to nanohybrid cellulose microspheres: dissolution, regeneration, functional properties and water remediation

Joana C. Almeida [a], William M. Facchinatto [a], Vasco Valente [a], Gabriela J. Campos [a], Denis Alikin [b], Andrei Kholkin [b,c], Nicolas Schaeffer [a], Armando J.D. Silvestre [a], Fátima Jesus [d], Joana L. Pereira [d], Adelaide Almeida [d], Carmen S.R. Freire [a], Carla Vilela [a,*]

[a] CICECO – Aveiro Institute of Materials, Department of Chemistry, University of Aveiro, Aveiro, 3810-193, Portugal
[b] CICECO – Aveiro Institute of Materials, Department of Physics, University of Aveiro, Aveiro, 3810-193, Portugal
[c] Institute of Solid State Physics, University of Latvia, Riga, LV-1063, Latvia
[d] CESAM – Centre for Environmental and Marine Studies, Department of Biology, University of Aveiro, Aveiro, 3810-193, Portugal

ARTICLE INFO

*Keywords:*
Cellulose
Organic electrolyte solution
Motile nanohybrid microspheres
Antibacterial activity
Non-ecotoxicity
Organic dye removal

ABSTRACT

Cellulose is a copious natural polymer that is being investigated to generate micro and nanoparticles with potential to address the challenge of water pollution. Herein, nanohybrid cellulose microspheres were developed, characterized and tested as advanced tools for water remediation. The microspheres were fabricated via dissolution of wood pulp fibers in an organic electrolyte solution followed by regeneration in water. Afterwards, nanohybrid cellulose microspheres were assembled via sequential *in situ* synthesis of inorganic nanoparticles (NPs), namely gold (AuNPs), platinum (PtNPs), and iron oxide ($Fe_3O_4$NPs). Nanohybrid microspheres (diameter of 680 ± 5 μm (dry state)) showed a content of 207 ± 5 μg $g^{-1}$ of Au, 649 ± 64 μg $g^{-1}$ of Pt and 59.7 ± 0.6 mg $g^{-1}$ of Fe. These microspheres can move via catalytic-powered and magnetic mechanisms, and can be easily recovered with a magnet. Moreover, they demonstrated antibacterial activity against methicillin-resistant *Staphylococcus aureus* (MRSA), and are non-ecotoxic towards *Raphidocelis subcapitata* and *Aliivibrio fischeri*. The Cell/Au–Pt–$Fe_3O_4$NPs microspheres were also able to remove model water-soluble dyes, namely methylene blue and methyl orange, reducing their concentration by ca. 67 and 37%, respectively, with the possibility of being reused. Overall, the obtained results show that these nanohybrid cellulose microspheres can effectively move and treat water contaminated with bacteria (MRSA) and organic pollutants, representing a sustainable solution for water remediation.

## 1. Introduction

The ubiquity of cellulose, together with its singular features, makes this natural polymer an inexhaustible resource for the development of environmentally conscious and sustainable materials [1,2]. Nevertheless, the strong intra- and intermolecular hydrogen bonds that govern the assembly of cellulose chains into fibers are the major culprit of the limited solubility of this polysaccharide in most conventional solvents, which restricts its widespread applicability as a natural resource for biobased materials development [3,4]. Common strategies to overcome this constraint are based on the chemical modification of cellulose into soluble derivatives (*e.g.*, cellulose acetate (CA) and carboxymethyl cellulose (CMC)) or the dissolution of cellulose with environmentally hazardous chemicals and solvents (e.g., the highly toxic carbon disulfide and the explosive *N*-methylmorpholine *N*-oxide (NMMO)) [5].

Aligned with the global emphasis on environmentally sustainable and safe methods for cellulose dissolution and processing, advancements have been made by employing ionic liquids (ILs) [6,7] and deep eutectic solvents (DES) [8,9], demonstrating promising potential for greener technologies. Despite the green connotation of ILs, they have some challenging characteristics that can be reduced by using an organic electrolyte solution (OES), *viz.* a mixture of a room-temperature IL with a neutral, organic and polar co-solvent (*e.g.*, dimethyl sulfoxide (DMSO)) [10–12]. In fact, the presence of the co-solvent increases the rate of cellulose dissolution due to the higher solvating power of ILs in the OES, decreases the viscosity of the obtained solutions and reduces the costs associated with the ILs [12].

After dissolution, cellulose can be regenerated in the form of (micro)

* Corresponding author.
*E-mail address:* cvilela@ua.pt (C. Vilela).

https://doi.org/10.1016/j.mtchem.2026.103801
Received 16 January 2026; Received in revised form 16 June 2026; Accepted 17 June 2026
Available online 23 June 2026
2468-5194/© 2026 The Authors. Published by Elsevier Ltd. This is an open access article under the CC BY-NC license (http://creativecommons.org/licenses/by-nc/4.0/).

fibers [13] for textile applications [14,15], films [16], and hydrogels for food packaging [17], or particles at the micro and nanoscales for drug delivery, cell culture, and tissue engineering [18,19]. In the realm of cellulose particles, several commercial microparticles are already available [18]. Notably, Cellufine™ comprises cellulose spherical beads with approximately 40–130 μm in diameter, primarily used as chromatography media [20]. Additionally, the Macroporous Bead Cellulose MT consists of highly porous regenerated cellulose particles ranging from about 30 to 250 μm, which are used as gel filtration media for biomolecule separation [21]. Another area of application is water remediation, where recent studies explored the use of cellulose-based microparticles (also named microbeads or microspheres) for the adsorption and removal of metal ions and organic dyes [22]. However, many of these approaches involve complex, time-consuming fabrication procedures along with multiple functionalization steps [23] or even necessitate extensive post-processing, which can limit their practicality and scalability [22]. Furthermore, most of the available literature on cellulose microspheres make use of dissolving grade pulp fibers, *viz*. high purity cellulose that dissolves in specific solvent systems, such as a mixture of lithium chloride and *N*,*N*-dimethylacetamide [24,25], or cellulose derivatives, such as CMC, which is soluble in water [26].

To the best of our knowledge, and despite the tremendous potential of cellulose-based materials for water remediation [27–29], there are no studies dealing with the use of regenerated nanohybrid cellulose microspheres, where wood pulp fibers from the pulp and paper industry and OES systems with a green connotation are used to increase the sustainability metrics of the ensuing materials. Moreover, the simple combination with inorganic nanoparticles (NPs), namely gold (AuNPs), platinum (PtNPs) and iron oxide ($Fe_3O_4$NPs) [30], can impart the cellulose microspheres with relevant functions in the context of water remediation, namely antibacterial activity, catalytic-powered movement, magnetic features and dye removal capacity.

In this sense, the present study aims to propose a strategy for the fabrication of multifunctional cellulose-based nanohybrid microspheres that can effectively move and treat water contaminated with bacteria and organic pollutants, representing a sustainable solution for water remediation. The cellulose microspheres were fabricated via dissolution of wood pulp fibers in an OES, namely 1-ethyl-3-methylimidazolium acetate ([Emim][OAc]) and dimethyl sulfoxide (DMSO), followed by regeneration in water, and decoration with AuNPs, PtNPs and $Fe_3O_4$NPs via the *in situ* reduction of their respective metal salts. The nanohybrid cellulose microspheres were studied regarding composition, structure, morphology and size, magnetic properties, mechanical performance, thermal stability, antibacterial action against a methicillin-resistant *Staphylococcus aureus* bacterium (MRSA), aquatic ecotoxicity towards the microalgae *Raphidocelis subcapitata* and the marine bacterium *Aliivibrio fischeri*, and removal of ionic organic model dyes.

## 2. Materials and methods

### 2.1. Chemicals, materials and microorganisms

Ammonium hydroxide solution ($NH_4OH$, 28.0-30.0% $NH_3$ basis), chloroplatinic acid hexahydrate ($H_2PtCl_6{\cdot}6H_2O$, ≥37.5% Pt basis), dimethyl sulfoxide (DMSO), 1-ethyl-3-methylimidazolium acetate ([Emim][OAc], ≥95.0%), hydrogen peroxide ($H_2O_2$, 30% (w/w) in water), iron (III) chloride hexahydrate ($FeCl_3{\cdot}6H_2O$, 97%), iron (II) chloride tetrahydrate ($FeCl_2{\cdot}4H_2O$, 99.0%), methyl orange (MO, dye content of 85%), methylene blue (MB, dye content of 70%), phosphate buffer saline (PBS, pH 7.4), sodium borohydride ($NaBH_4$, ≥98%), tetrachloroauric (III) acid trihydrate ($HAuCl_4{\cdot}3H_2O$, 99.9%), trisodium citrate dihydrate ($Na_3C_6H5O_7{\cdot}2H_2O$, ≥99%) and yttrium (III) chloride ($YCl_3$, 1000 ppm Certipur® standard) were purchased from Sigma-Aldrich (St. Louis, MO, USA). Tryptic soy agar (TSA) and tryptic soy broth (TSB) were supplied by Liofilchem (Roseto degli Abruzzi TE, Italy). Ultrapure water (Type 1, resistivity = 18.2 MΩ cm at 25 °C) was obtained by a Simplicity® Water Purification System (Merck, Darmstadt, Germany). Other chemicals and solvents were of laboratory grade and used as received without any further purification.

Bleached kraft eucalyptus cellulose pulp with a crystallinity index of *ca*. 77%, molecular weight of *ca*. 270 kDa, and average dimensions of 770 ± 6 μm of length and 18.2 ± 0.1 μm of width was kindly provided by a Portuguese pulp mill (Figueira da Foz, Portugal): solid-state $^{13}C$ CP/MAS NMR (B0 field of 9.4 T, 12 kHz MAS with proton 90° pulse of 3 μs, time between scans of 3 s, contact time of 2000 μs, Bruker Avance III 400 spectrometer (Billerica, MA, USA)) with resonances at δ 65.1 ppm (C6), 71.3–74.2 ppm (C2,3,5), 90.1 ppm (C4) and 104.8 ppm (C1).

Methicillin-resistant *S. aureus* (MRSA, DSM 25693) bacterium was provided by DSMZ – Deutsche Sammlung von Mikroorganismen und Zellkulturen GmbH (German Collection of Microorganisms and Cell Cultures). The green microalga *R. subcapitata* strain (NIES-35) was acquired from Culture Collection of Algae and Protozoa (CCAP, UK). The bacterium *A. fischeri* (DSM 7151) was provided lyophilized as part of the Microtox® Toxicity Test kit (Modern Water Inc, USA).

### 2.2. Cellulose dissolution and regeneration into microspheres

Cellulose dissolution was investigated for different concentrations of cellulose (1.5 and 3.0 wt%) and mass fractions of [Emim][OAc]:DMSO (50:50, 40:60, 30:70, 25:75, and 20:80), as summarized in Section I of the Supplementary Material. In short, the cellulose solutions were prepared by adding the adequate amount of cellulose fibers to the corresponding content of OES (Table S1) under magnetic stirring for 3 h at 27 °C.

The regeneration of the dissolved cellulose into microspheres was achieved by adding dropwise each of the previous cellulose solutions to a large volume of the anti-solvent (water) at room temperature. Various parameters, namely the concentration (1.5 and 3.0 wt%) and volume (0.2 and 2.0 mL) of the cellulose solution, the volume (5.0, 10.0 and 20.0 mL) and stirring speed (0, 500 and 1250 rpm) of the anti-solvent, the syringe needle gauge (0.30 and 0.45 mm) and the syringe pump flow rate (0.1, 0.2 and 0.5 mL $min^{-1}$), were studied to optimize the production of the cellulose microspheres, as outlined in Section II of the Supplementary Material. Briefly, the optimized regeneration process started by placing 2.0 mL of the cellulose solution (3 wt%) in a syringe with a needle gauge of 0.45 mm and adding it dropwise at a flow rate of 0.1 mL $min^{-1}$ by a syringe pump (PHD ULTRA™ Syringe Pump, Harvard Apparatus, Massachusetts, USA) to 20.0 mL of water (anti-solvent) stirring at 1250 rpm. After regeneration, the cellulose microspheres (i.e., Cell) were washed three times with ultrapure water during 24 h under mechanical shaking and were kept in ultrapure water until further use or allowed to dry under ambient conditions for characterization.

### 2.3. Preparation of the nanohybrid cellulose microspheres (Cell/Au–Pt–$Fe_3O_4$NPs)

Nanohybrid cellulose microspheres were prepared via the sequential *in situ* synthesis of the AuNPs, PtNPs and $Fe_3O_4$NPs in the presence of the cellulose microspheres. This methodology was selected after optimization, as compiled in Sections III and IV of the Supplementary Material. Briefly, a suspension of cellulose microspheres (*ca*. 10.0 mg) was added to an $HAuCl_4$ aqueous solution (10.0 mL, 0.24 mM) [31]. Then, an aqueous solution of sodium citrate (188 μL, 85 mM) was added to the mixture. Reduction of the gold salt complex was carried out in a microwave reactor (Anton Paar Monowave 300, Graz, Austria) at 120 °C during 1 min. The obtained suspension was centrifuged (Thermo-Scientific Megafuge 16R Centrifuge, Massachusetts, USA) for 30 min at 15,000 rpm and 4 °C and washed three times with ultrapure water.

The singly functionalized microspheres (i.e., Cell/AuNPs) were resuspended in ultrapure water and added to an aqueous solution of $H_2PtCl_6$ (9.5 mL, 16 mM) and sodium citrate (0.25 mL, 40 mM) [32]. The solution was stirred for 30 min at room temperature, after which

$NaBH_4$ (50 μL, 50 mM) was added dropwise to the mixture. The suspension was allowed to react at ambient temperature during 1 h. Finally, the obtained suspension was centrifuged for 1 h at 15,000 rpm and 4 °C, and washed three times with ultrapure water.

The doubly functionalized microspheres (i.e., Cell/Au-PtNPs) were resuspended in ultrapure water and added to 10.0 mL of a degassed aqueous solution of $Fe^{2+}$ (50 mM) and $Fe^{3+}$ (100 mM) and maintained in a nitrogen atmosphere under stirring at 80 °C [33]. Precipitation occurred after addition of a $NH_4OH$ solution (1.0 μL, 25%). The mixture was allowed to react for 1 h. The final suspension was centrifuged for 1 h at 15,000 rpm and 4 °C and washed three times with ultrapure water. The nanohybrid microspheres (i.e., Cell/Au–Pt–$Fe_3O_4$NPs) were resuspended in ultrapure water and stored at room temperature until further use or allowed to dry under ambient conditions prior to characterization.

### 2.4. Characterization methods

#### 2.4.1. Attenuated total reflection-fourier transform infrared (ATR-FTIR) spectroscopy

ATR-FTIR spectra were recorded with a PerkinElmer FT-IR System Spectrum BX spectrophotometer (PerkinElmer Inc., Massachusetts, USA) equipped with a single horizontal Golden Gate ATR cell, over the range of 600–4000 $cm^{-1}$ at a resolution of 4 $cm^{-1}$ over 32 scans.

#### 2.4.2. X-ray diffraction (XRD)

XRD was performed on a Phillips X'pert MPD diffractometer (PANalytical, Eindhoven, Netherlands) using Cu Kα radiation (λ = 1.541 Å) with a scan rate of 0.05° $s^{-1}$. The XRD patterns were collected in reflection mode with the test specimens (flat discs with 1.5 $cm^2$) placed on a Si wafer (negligible background signal) for mechanical support.

#### 2.4.3. Optical microscopy

Optical micrographs were recorded with an OLYMPUS BX51 optical microscope (Olympus Europa, Hamburg, Germany) coupled with a digital uEye camera (IDS Imaging Development Systems, Obersulm, Germany), or with a Nikon SMZ18 stereomicroscope (Nikon SMZ18, Tokyo, Japan) coupled with a SRH Plan Apo 2 camera (Nikon, Tokyo, Japan).

#### 2.4.4. Scanning electron microscopy (SEM) coupled with energy dispersive X-ray spectroscopy (EDS)

SEM micrographs were obtained by using a HR-FESEM SU-70 Hitachi microscope (Hitachi High-Technologies Corporation, Tokyo, Japan) operating at 15 kV. The microscope was equipped with an EDS microanalysis Bruker QUANTAX 400 detector (Bruker Nano GmbH, Berlin, Germany) to perform the elemental analysis (C, O, Au, Pt and Fe) and elemental mapping (15 kV). The samples were placed on an aluminum plate using carbon tape and previously coated with a carbon film. The average size was determined with a minimum of 100 measurements using the Fiji image software.

#### 2.4.5. Atomic force microscopy (AFM)

Topography, magnetic and mechanical properties were measured using an Ntegra Prima scanning probe microscope (NT-MDT, Apeldoorn, The Netherlands) under dry-air conditions maintained by a continuous gas flow. Topography and magnetic force microscopy (MFM) images were acquired using MagneticMulti75-G probes (Budget Sensors, Sofia, Bulgaria) with a nominal tip radius of 60 nm and a spring constant of approximately 5 N $m^{-1}$. The arithmetical mean height of the surface ($S_a$) was calculated using Gwyddion software from topography images obtained in tapping mode. MFM images were collected in lift mode with a second-pass lift distance of approximately 50 nm.

Mechanical properties, including Young's modulus (E) and adhesion ($F_{adh}$), were evaluated from force-distance curves acquired using D160 single crystal diamond probes (K-TEK Nanotechnology, Wilsonville, USA) with a nominal tip radius of 10 nm. Cantilever spring constants of 10-15 N $m^{-1}$ were determined using the Lübbe method [34], which relies on optical measurements of cantilever width and length, as well as the positions of the first and second flexural resonance modes. The force-distance curves were used to recalculate the dependence of the force on indentation depth, which further has been fitted by Derjaguin-Muller-Toporov Model (DMT) to extract E and $F_{adh}$.

#### 2.4.6. Total reflection X-ray fluorescence (TXRF) spectrometry

The metal content (Au, Pt and Fe) was analyzed on a TXRF Bruker S2 Picofox spectrometer with a molybdenum X-ray source (Bruker Corporation, Billerica, MA, USA). The voltage of the X-ray tube was 50 kV, the current 600 μA and the acquisition time was set at 500 s. Prior to TXRF analysis, the cellulose microspheres loaded with the inorganic NPs were digested in 1.0 mL of concentrated aqua regia (ratio of 3:1 of HCl:$HNO_3$) at 70 °C for 2 h. After leaching, the solutions were centrifuged at 5000 rpm for 2 min and 0.5 mL of the supernatant was diluted to a known volume (either 5.0 mL or 10.0 mL) in a volumetric flask. All silica sample carriers were first treated with 10.0 μL of silicon in isopropanol solution and dried at 80 °C for 30 min. The diluted samples were spiked with a known volume of a 1000 ppm $YCl_3$ standard to obtain a final standard element concentration of 1 to 10 ppm (mg $L^{-1}$), depending on the sample metal content. Ten microliters of each solution containing the metals and the yttrium standard were added onto a treated carrier and dried on a hot plate at 80 °C for 30 min.

#### 2.4.7. Thermogravimetric analysis (TGA)

TGA was performed with a Hitachi STA300 TGA analyzer (SETARAM Instrumentation, Lyon, France) equipped with a platinum cell. The test specimens were heated from room temperature to 800 °C, at a constant rate of 10 °C $min^{-1}$ under inert ($N_2$) atmosphere.

### 2.5. Mobility (catalytic and magnetic) tests

Propulsion tests were conducted by immersing the nanohybrid cellulose microspheres (*i.e.*, Cell/Au–Pt–$Fe_3O_4$NPs) in an aqueous solution of hydrogen peroxide (10% w/v). Approximately 20.0 mL of the $H_2O_2$ aqueous solution was placed in a Petri dish and a microsphere was then gently introduced into the solution. The system was left undisturbed, and the motion of the microsphere was monitored with a digital camera (UI-1240ML-C-HQ, IDS Imaging Development Systems GmbH, Obersulm, Germany) to obtain time-lapse images to evaluate its propulsion behavior.

Magnetic motion tests were performed by placing a magnet underneath a Petri dish containing the Cell/Au–Pt–$Fe_3O_4$NPs nanohybrid and also observed with a digital camera to acquire time-lapse images.

### 2.6. In vitro antibacterial activity

The nanohybrid cellulose microspheres were tested for antibacterial activity against a multi-drug resistant *S. aureus* strain. Prior to the assay, all microspheres were sterilized with ultraviolet light (UV-C) (Voltex, UVX) for 20 min. The bacteria were grown on a solid medium (TSA) at 37 °C for 24 h and then stored at 4 °C. An isolated colony was inoculated into 30.0 mL of TSB medium and incubated aerobically at 25 °C with shaking at 120 rpm for 24 h. An aliquot of 300 μL was transferred to fresh TSB medium and incubated under the same conditions until the stationary phase was reached (≈$10^9$ colony-forming units (CFU) $mL^{-1}$). The bacterial culture was diluted in PBS to achieve a concentration of $10^5$ CFU $mL^{-1}$ and incubated with the samples at 25 °C. At 0, 24, 48 and 72 h of incubation, 100 μL aliquots were taken, diluted in PBS, and plated using the drop plate method (two drops of 10 μL per dilution) on TSA medium. The plates were incubated at 37 °C for 24 h, and the bacterial concentration (CFU $mL^{-1}$) was determined by counting colonies in the most appropriate dilution. Each experiment was conducted in triplicate.

For the reusability tests, the microspheres were removed from the media, thoroughly washed with ultrapure water, sterilized using ultraviolet light for 20 min, and then subjected to the same testing procedures as described previously.

### 2.7. Aquatic ecotoxicity

#### 2.7.1. Ecotoxicity assays with freshwater microalgae

To evaluate the potential ecotoxicity associated with the use of the Cell/Au–Pt–$Fe_3O_4$NPs microspheres, a growth inhibition assay was performed with the freshwater green microalgae *R. subcapitata*. The test followed the OECD Guideline 201 [35], adapted for 24-well microplates [36].

An inoculum was prepared 4 days in advance from a non-axenic culture of the microalgae cyclically maintained in the laboratory in Woods Hole MBL medium under controlled conditions (23 ± 1 °C, $16h^L$:$8h^D$ photoperiod) [37]. At the start of the assay, microalgae were inoculated into each well at an initial density of $1.0 \times 10^4$ cells $mL^{-1}$. Test solutions consisted of ultrapure water that had been previously in contact with Cell/Au–Pt–$Fe_3O_4$NPs for 2 h under agitation (250 rpm) at room temperature. After this contact period, the samples were tested at the following dilutions: 100%, 50%, 25%, 10%, and 5% (v/v in ultrapure water). To ensure nutrient sufficiency throughout the test period, all samples were supplemented with a concentrated nutrient stock, bringing them to the equivalent of standard MBL medium concentrations. The addition of the microalgae suspension and the nutrient spiking solution caused a slight dilution of the test samples, leading to each sample being tested at 98.2% strength. Each condition was tested in triplicate, including a control group composed of nutrient-spiked ultrapure water with microalgae. The total volume per well was fixed at 1.0 mL. Microplates were incubated for 96 h under constant illumination at 23 ± 1 °C. Algal growth was quantified spectrophotometrically at 440 nm at the end of the exposure period. Absorbance values were converted to cell density using a previously constructed calibration curve. Biomass yield (cells $mL^{-1}$) was calculated as the difference in cell density between the beginning and the end of the test. Yield inhibition was expressed as a percentage relative to the control yield (percentage inhibition in yield).

#### 2.7.2. Ecotoxicity assays with marine bacteria

A bioluminescence inhibition assay was performed to assess the toxicity of the water that had been in contact with Cell/Au–Pt–$Fe_3O_4$NPs, using the same sample and dilutions as above mentioned. The test was conducted using the marine bioluminescent bacterium *A. fischeri*, with luminescence measurements performed on a Microtox® 500 Analyzer (Modern Water Inc, USA). The assay was based on the inhibition of bacterial luminescence, following the Whole Effluent Toxicity (WET) test [38]. Each dilution was adjusted to 2% (w/v) NaCl, which was dissolved in the test solution to provide optimal conditions for the marine bacteria. Lyophilized *A. fischeri* cultures stored at −20 °C were reconstituted immediately before use according to the manufacturer's instructions. For each condition, 10 μL of the rehydrated bacterial suspension was added to 1000 μL of the test solution, leading to each sample being tested at 99.0% strength. Bioluminescence was measured at 15 and 30 min after the start of exposure at 15 °C. A control, consisting of 2% NaCl in ultrapure water without any prior contact with the hybrid particles, was included to define baseline luminescence. The percentage of luminescence inhibition was calculated relative to the control response. All conditions were tested in duplicate to ensure reproducibility.

### 2.8. Dye removal tests

The nanohybrid cellulose microspheres were placed in 5.0 mL of the dye solutions with a concentration of 25 mg $L^{-1}$ of MO and MB in the presence of 0.1 M of $H_2O_2$ [39]. The pH was adjusted to 4 for MO and 6 for MB with aqueous solutions of HCl (0.1 M) and NaOH (0.1 M), respectively. For each condition, the dyes removal was confirmed by UV-Vis spectroscopy (Shimadzu UV1800 UV-Vis spectrophotometer, Shimadzu Corporation, Kyoto, Japan) with the following calibration curves for MO (464 nm): $y = 0.0703x - 0.0004$ ($R^2 = 1.0000$), and for MB (664 nm): $y = 0.1962x + 0.0375$ ($R^2 = 0.9992$). The first absorbance measurement was obtained right after the addition of the microspheres, and then after 10, 20, 30, and 120 min under constant mechanical shaking at room temperature. The reusability of the nanohybrid cellulose microspheres was tested for two more cycles of removal in the same conditions after washing them with ultrapure water for 72 h under constant stirring.

### 2.9. Statistical analysis

Statistical significance was established at $p < 0.05$ using two-way variance analysis (ANOVA) and Tukey's test (GraphPad Prism 8.0, GraphPad Software, San Diego, CA, USA).

## 3. Results and discussion

Nanohybrid cellulose microspheres were fabricated via dissolution of wood pulp fibers in an OES, followed by regeneration in water (Fig. 1A) and functionalization with AuNPs, PtNPs and $Fe_3O_4$NPs (Fig. 1B). Wood pulp fibers were selected for their renewability, abundance, low cost and fascinating properties [40], while the OES, formed by 1-ethyl-3-methylimidazolium acetate ([Emim][OAc]) and dimethyl sulfoxide (DMSO), was chosen for its versatility in the dissolution and regeneration of cellulose [12]. Furthermore, cellulose was regenerated into microspheres because of their large surface area and the abundance of surface hydroxyl groups that enable a variety of physical and chemical modifications, including coating with metal or metal oxide NPs [18, 30]. Lastly, the AuNPs, PtNPs, and $Fe_3O_4$NPs were carefully selected to impart the microspheres with antibacterial action, catalytic propulsion, and magnetic features, respectively.

As a proof-of-concept, the functional nanohybrid cellulose microspheres were studied regarding their catalytic-powered and magnetically controlled movement, antibacterial activity against the MRSA harmful bacteria, and aquatic ecotoxicity towards the freshwater microalgae *R. subcapitata* and the marine bacterium *A. fischeri*. Furthermore, their ability to remove toxic model organic dyes, namely MB and MO, was also investigated.

### 3.1. Cellulose dissolution and regeneration into microspheres

#### 3.1.1. Cellulose dissolution

The dissolution process of cellulose in the OES, constituted by the ionic liquid [Emim][OAc] and the neutral, organic and polar co-solvent DMSO, was investigated for solutions containing different concentrations of cellulose, *viz.* 1.5 and 3.0 wt%, and distinct mass ratios of [Emim][OAc] and DMSO, namely 50:50, 40:60, 30:70, 25:75, and 20:80 (Section I, Table S1, Supplementary Material). It is important to note that the dissolution tests were performed at a low temperature as a strategy to reduce the production costs and to facilitate scale-up, despite the intrinsic lower rate of cellulose dissolution [11].

The digital photographs of the various cellulose solutions (Fig. S1A) clearly show that the wood pulp fibers are soluble in the OES system up to mass ratios of 25:75, since the solutions are clear and transparent. In the case of the 20:80 mass ratio, a turbid suspension was obtained for both cellulose concentrations, thus, demonstrating a lower solubility of this polysaccharide. This is corroborated by the optical micrographs of the various cellulose solutions (Fig. S1B), where only the samples Cell1.5_20:80 and Cell3_20:80 display the presence of fibers that were not completely dissolved. The analysis of the cellulose solutions by ATR-FTIR spectroscopy (Fig. S2) mainly shows the characteristic absorption bands of the OES system, namely at 1574 $cm^{-1}$ assigned to the C=N=

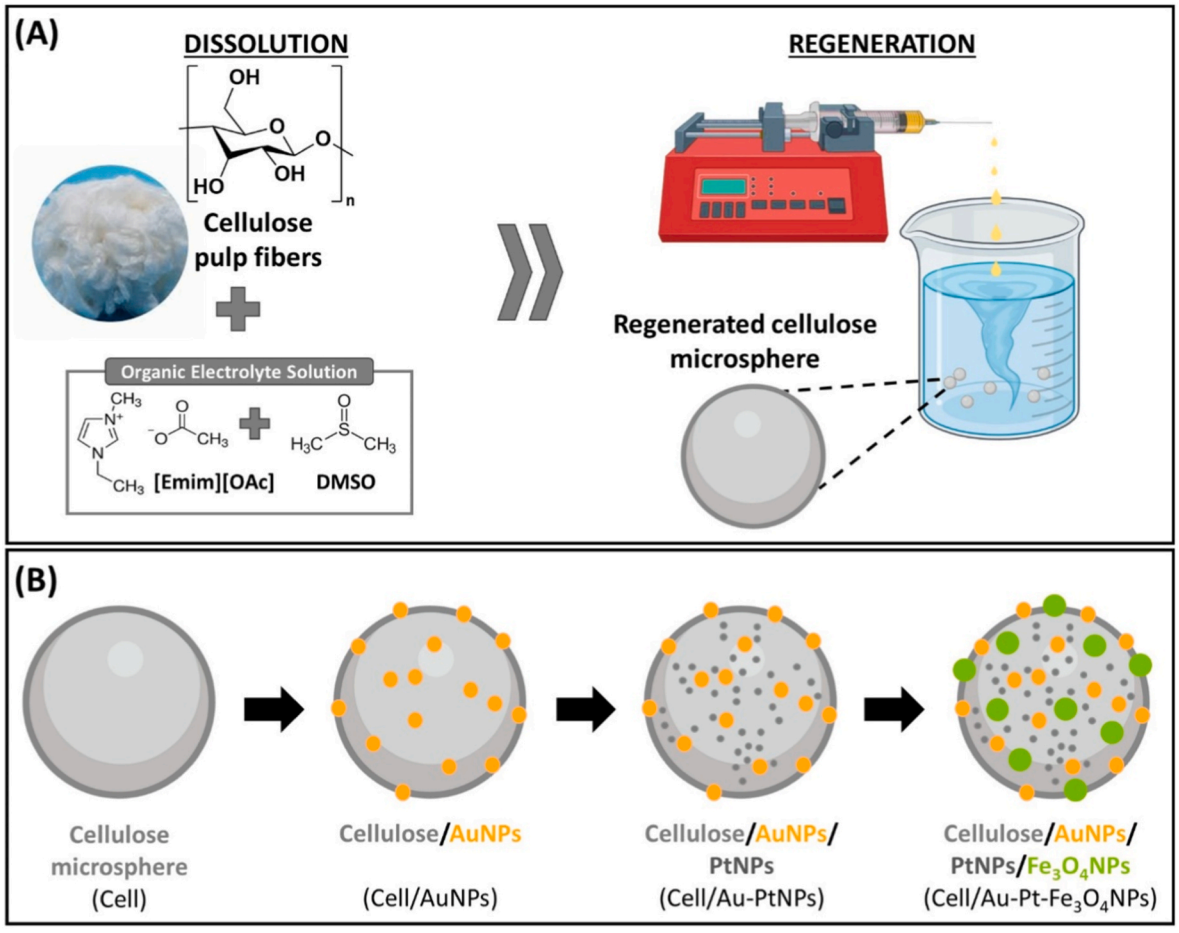


**Fig. 1.** Schematic illustration of the fabrication of the nanohybrid cellulose microspheres: (**A**) cellulose dissolution and regeneration into microspheres via batch syringe extrusion, and (**B**) sequential *in situ* assembly of the inorganic nanoparticles into the cellulose microspheres.

bond of [Emim][OAc] and at 1030 $cm^{-1}$ allocated to the S═O═ bond of DMSO [41], which is in tune with the low contents of cellulose. The similarity between the spectra of the cellulose solutions and that of the pure OES in most of the spectral regions was also reported for microcrystalline cellulose (MCC) dissolved in [Emim][OAc] [42]. These results demonstrate that the selection of wood pulp fibers as an alternative and readily available source of cellulose rather than dissolving-grade pulp [24] together with the use of an OES system instead of conventional toxic solvents [25], is an effective approach to obtain cellulose solutions with lower environmental impact.

The suitability of these cellulose solutions for the regeneration process via solvent displacement method was evaluated by analyzing their rheological performance. According to Fig. S3A, the shear viscosity of all cellulose solutions decreased as the shear rate increased, demonstrating a shear-thinning behavior. Moreover, as anticipated, the addition of a co-solvent, namely DMSO, induced an exponential decline of the viscosity of cellulose solutions. This is further corroborated by the elastic ($G'$) and viscous ($G''$) moduli data (Fig. S3B), where $G'$ is always smaller than $G''$ for the entire frequency range, which indicates that all solutions present a behavior that is more liquid than solid [43], confirming their aptness for the dropwise extrusion via a syringe needle assisted by a syringe pump (Fig. 1A).

### 3.1.2. *Cellulose regeneration into microspheres*

The regeneration of the previously dissolved cellulose fibers into microspheres was performed in water because, according to literature, cellulose regenerated with water as anti-solvent from [Emin][OAc] shows a higher thermal stability than using ethanol or a mixture of water and ethanol [44]. Furthermore, the mechanical properties are also affected by the type of anti-solvent used to produce cellulose beads or microspheres obtained from dissolving grade pulp in a mixture of lithium chloride and *N*,*N*-dimethylacetamide followed by regeneration in water or ethanol [45].

Various parameters were studied for the regeneration of cellulose in water (see Section II, Supplementary Material). After optimization, the cellulose solution with a mass ratio of 25:75 of [Emim][OAc]:DMSO, which corresponds to a molar ratio of 13:87 of [Emim][OAc]:DMSO, was the most satisfactory proportion regarding efficient dissolution and suitable viscosity for syringe extrusion, and was the one that gave better results in terms of shape and size homogeneity of the microspheres (Fig. S4). Therefore, the cellulose microspheres regenerated from the Cell3_25:75 solution (Table S1) and dried under ambient conditions (Fig. S5) were selected for the next steps, and were characterized by ATR-FTIR spectroscopy, XRD, TGA, optical microscopy, SEM, and AFM.

The ATR-FTIR spectrum (Fig. 2A) of the cellulose microspheres exhibits the characteristic bands of a cellulosic substrate, namely at 3337 $cm^{-1}$ (stretching vibration of the OH groups), 2898 $cm^{-1}$ (C–H stretching vibrations of CH and $CH_2$ groups), 1159 $cm^{-1}$ (antisymmetric stretching vibration of the C–O–C glycosidic bonds), and at 1104, 1052 and 1029 $cm^{-1}$ (stretching vibrations of the C–O bond of carbons 2, 3 and 6) [46]. As anticipated, the ATR-FTIR spectrum of the cellulose microspheres is analogous to that of the wood cellulose pulp fibers, showing that no chemical reactions occurred during the physical dissolution and regeneration of cellulose [47]. Worth noting is also the fact that the typical absorption bands of [Emim][OAc] (═C═N bond at 1574 $cm^{-1}$) and DMSO (═S═O at 1030 $cm^{-1}$) are not present in the

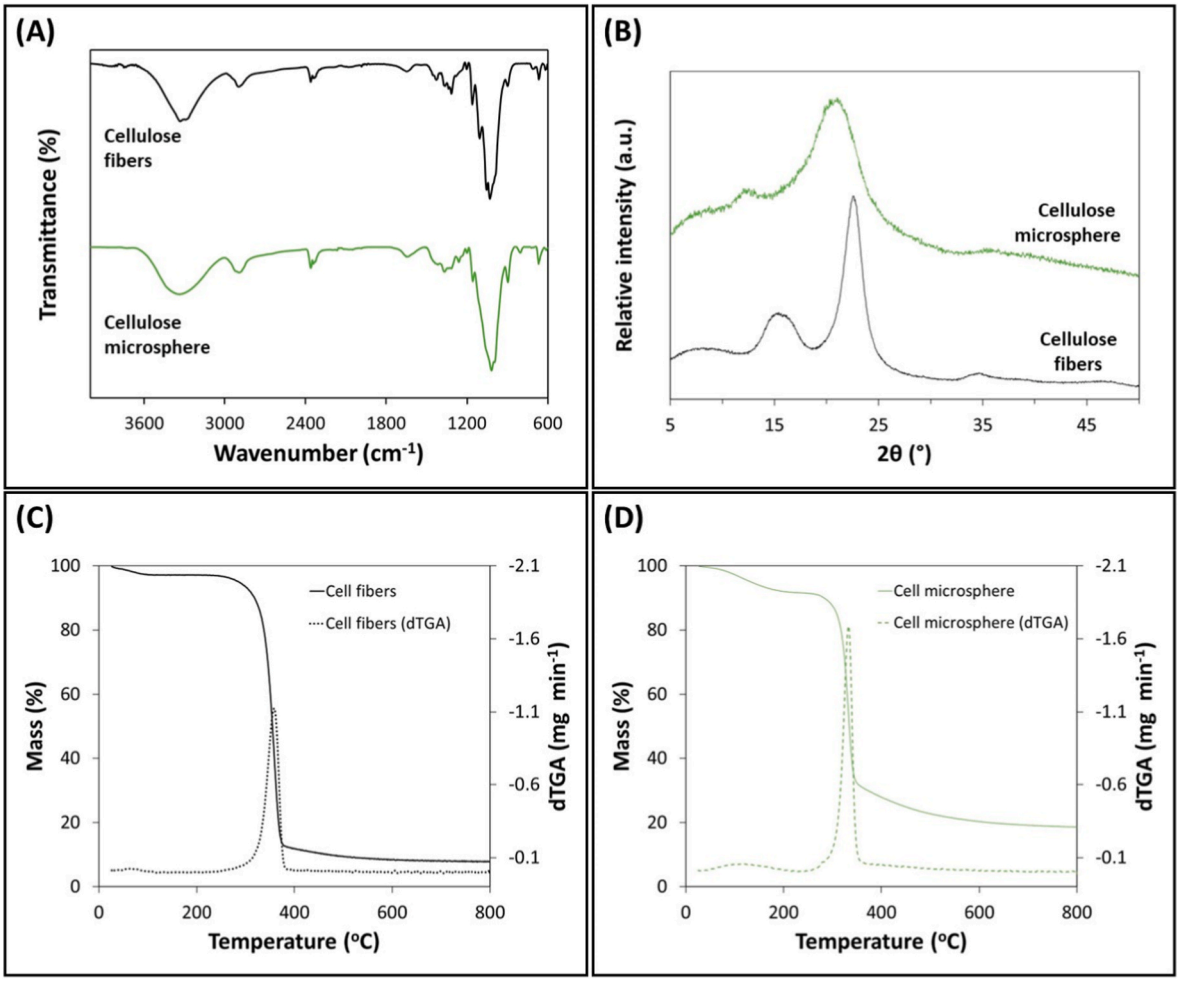


**Fig. 2.** (**A**) ATR-FTIR spectra, (**B**) XRD diffractograms, (**C,D**) TGA and derivative curves of the wood cellulose fibers and the microspheres generated from a cellulose solution with a mass ratio of 25:75 of [Emim][OAc]:DMSO.

ATR-FTIR spectrum of the cellulose microspheres, which demonstrates that the solvent and co-solvent were effectively removed during the regeneration and washing processes.

The diffractogram of the cellulose microspheres (Fig. 2B) presents a small broad peak centered at $2\theta = 12.2^{\circ}$ allocated to the (1 $\bar{1}$ 0) diffraction plane and two overlapped broad peaks at $2\theta = 20.4^{\circ}$ and $21.5^{\circ}$ assigned to the (110) and (020) diffraction planes [48–50], which are characteristic of regenerated cellulose with a diffraction pattern of cellulose II. Contrary, the cellulose fibers diffractogram shows peaks at $2\theta$ $15.5^{\circ}$, $16.2^{\circ}$ and $22.4^{\circ}$, allocated to the (101), (10 $\bar{1}$) and (002) diffraction planes, respectively, typical of cellulose I [46]. So, as envisaged, there is a visible transition in allomorphs between the wood pulp fibers (cellulose I) and the cellulose microspheres (cellulose II) during the dissolution and regeneration processes [51].

In terms of thermal stability (Fig. 2C and D), the regenerated cellulose microspheres exhibit a decomposition profile cognate to that of wood cellulose fibers with a single mass-loss step as the result of the pyrolysis of the cellulose skeleton [52], although at lower maximum decomposition temperatures. Apart from the volatilization of water below 100 °C, the thermal degradation of the regenerated cellulose microspheres began at approximately 270 °C and reached a maximum at 331 °C, aligned with data reported elsewhere [14]. Therefore, the regenerated cellulose microspheres are less thermally stable than the starting wood pulp cellulose fibers, which might be credited to the chain disruption after dissolution, regeneration, and rearrangement of the cellulose crystal structure, as substantiated by the XRD data [41,44]. Nonetheless, the regenerated cellulose microspheres are still thermally stable up to about 250 °C, which can be a valuable property in the industrial context where the effluents can be warm or hot.

Fig. 3A shows that the cellulose microspheres are perfectly spherical and have an average diameter of 2.3 ± 0.5 mm and 680 ± 5 μm in the wet and dry states, respectively. So, upon drying under ambient conditions, the diameter of the microspheres decreased by a factor of about 3.38, while retaining their spherical shape. This shrinking behavior was also reported for cellulose beads or microspheres obtained via dissolution of dissolving grade pulp in a mixture of lithium chloride and *N*,*N*-dimethylacetamide followed by regeneration in water [25], ethanol [53] or water/ethanol mixtures [54]. Although the sizes of the cellulose microspheres in both wet and dry states are comparable to those reported in the literature [24,25], a key advantage of the microspheres produced in this study is the use of directly derived wood pulp fibers and ecofriendly solvent systems. This approach eliminates the need for dissolving grade pulp fibers (*e.g.*, Enocell) and the toxic solvents (*e.g.*, mixture of lithium chloride and *N*,*N*-dimethylacetamide) [24,25], making the process more sustainable and environmentally friendly.

Fig. 3B illustrates the surface AFM topography of the cellulose microspheres with a determined average $S_a$ value of 65 nm. So, the use of an OES ([Emim][OAc]:DMSO with 25:75 mass ratio) for cellulose dissolution followed by regeneration in water is a straightforward green approach to generate cellulose microspheres with nanoscale roughness. Previous studies also reported that regenerated cellulose beads/spheres (produced from a solution of Enocell dissolving grade pulp in *N*,*N*-dimethylacetamide/LiCl) with a diameter of 710 ± 10 μm can have

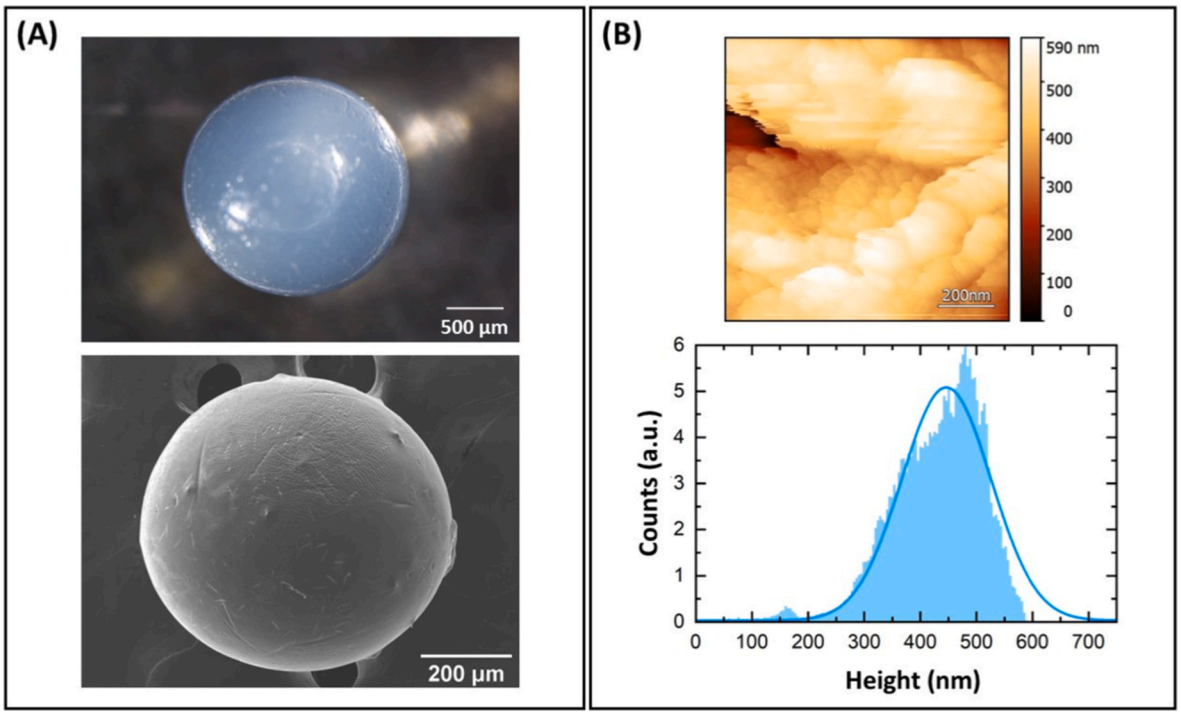


**Fig. 3.** (**A**) Optical (top, wet state) and SEM (bottom, dry state) micrographs, and (**B**) AFM topography (top) and height distribution (bottom) of the optimized microspheres generated from a cellulose solution with a mass ratio of 25:75 of [Emim][OAc]:DMSO.

surface roughness in the nanometer range [25].

Lastly, the mechanical properties of the cellulose microspheres were studied by indentation with a single-diamond probe. The local Young's modulus values varied from 500 to 2000 MPa across the entire microsphere, which indicates that some parts are more stiffer than others. These cellulose microspheres are stiffer than microbeads assembled from carboxylated cellulose nanocrystals (Young's modulus ~18 MPa, diameter <10 µm, spray-drying) [55] and regenerated cellulose beads from Domsjö dissolving pulp (Young's modulus ~ 12 MPa, diameter ~ 500 µm, cellulose content: 1 wt%) [45], but close to that of the regenerated cellulose beads from Enocell dissolving grade pulp (Young's modulus ~ 1800 MPa, diameter ~710 µm, cellulose content: 1.5 wt%) [25]. These differences in mechanical properties are credited to factors such as fabrication methodology, cellulose concentration and beads density and surface area, as well as the drying process as discussed elsewhere [45].

### 3.2. Assembly and characterization of the nanohybrid cellulose microspheres

After studying the dissolution of cellulose and the practicality of shaping it into microspheres, the next stage was to functionalize the regenerated cellulose microspheres with the inorganic nanoparticles. Two assembly methodologies were tested and optimized (Section III of the Supplementary Material, Fig. S6–S9, Table S2) to generate nanohybrid cellulose microspheres, as outlined in Fig. 1B. Upon the functionalization of the whitish cellulose microspheres via the sequential *in situ* synthesis of the inorganic NPs, the final suspension exhibited a dark coloration, which is conferred by the presence of the $Fe_3O_4$NPs on the surface of the cellulose microspheres.

#### 3.2.1. Composition, structure, morphology and topography

The elemental chemical composition of the nanohybrid cellulose microspheres was assessed by EDS analysis. Fig. 4A shows that all the EDS spectra of the microspheres display the binding energies of carbon (C) and oxygen (O) peaks at 0.27 and 0.53 keV [56], respectively, which is characteristic of cellulose. Additionally, all three samples (i.e., Cell/AuNPs, Cell/Au-PtNPs, and Cell/Au–Pt–$Fe_3O_4$NPs) present the typical peak of gold (Au) at 2.12 keV [57]. The presence of the PtNPs in the Cell/Au-PtNPs and Cell/Au–Pt–$Fe_3O_4$NPs microspheres is not clear, as the characteristic peak of this metal (binding energy of ca. 2.05 keV [58]) cannot be distinguished from that of Au in the EDS spectra since they overlap. The EDS spectrum of the Cell/Au–Pt–$Fe_3O_4$NPs hybrid also shows the peaks of iron (Fe) at 0.71, 6.40, and 7.07 keV [58], thus confirming the effective functionalization with the $Fe_3O_4$NPs.

The surface chemical composition of the Cell/Au–Pt–$Fe_3O_4$NPs nanohybrid was also assessed by EDS mapping for gold, platinum, and iron. According to Fig. 4B, each element is uniformly distributed across the surface of the Cell/Au–Pt–$Fe_3O_4$NPs nanohybrid. In terms of normalized element content (wt.%), the Cell/Au–Pt–$Fe_3O_4$NPs nanohybrid is composed of 22.9 ± 11.1% of carbon, 39.9 ± 16.9% of oxygen, 0.6 ± 0.2% of gold, 1.6 ± 0.3% of platinum, and 35.0 ± 3.7% of iron.

The quantification of the inorganic fraction in the Cell/Au–Pt–$Fe_3O_4$NPs was further determined by TXRF, showing a content of 207 ± 5 µg $g^{-1}$ of gold, 649 ± 64 µg $g^{-1}$ of platinum, and 59.7 ± 0.6 mg $g^{-1}$ of iron. These values are in line with the normalized contents of the Au, Pt, and Fe elements obtained by EDS.

The XRD diffractograms (Fig. 4C) of the Cell/AuNPs, Cell/Au-PtNPs, and Cell/Au–Pt–$Fe_3O_4$NPs nanohybrid microspheres reveal the characteristic broad peak of regenerated cellulose at approximately 2θ ≈ 20° and 21° [15]. This feature is most pronounced in the samples with lower content of inorganic nanoparticles, namely Cell/AuNPs and Cell/Au-PtNPs, consistent with the trend observed in the single nanohybrids (Cell/AuNPs and Cell/PtNPs, Fig. S8A, Supplementary Material). Moreover, the diffractogram of the Cell/Au–Pt–$Fe_3O_4$NPs nanohybrid displays distinct peaks at 2θ ≈ 30° (220), 36° (311), 43° (400), 53° (422), 57° (511) and 62° (440), corresponding to magnetite [59], alongside the diffraction pattern of cellulose II. The characteristic diffraction peaks of AuNPs (2θ ≈ 38° (111), 44° (200), 64° (220) and 78° (311)) and PtNPs (2θ ≈ 39° (111), 46° (200) and 67° (220)) [60] are likely overlapped or masked by the broader and more intense diffraction peaks of $Fe_3O_4$NPs. Similar observations were reported by Lau et al.

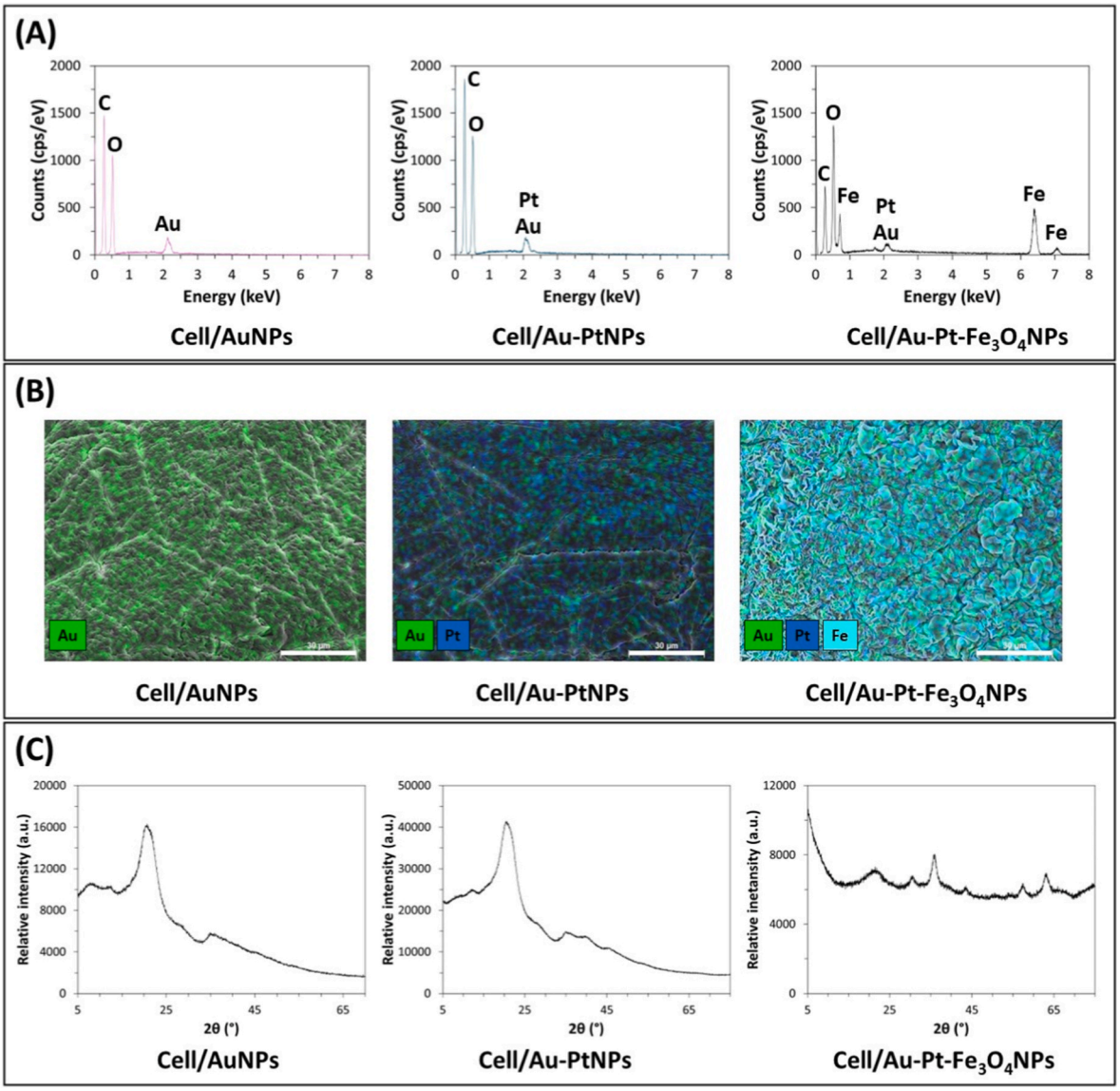


**Fig. 4.** (**A**) EDS spectra, (**B**) EDS mapping (scale bar: 30 μm), and (**C**) XRD diffractograms of the nanohybrid cellulose microspheres: Cell/AuNPs, Cell/Au-PtNPs and Cell/Au–Pt–$Fe_3O_4$NPs.

[61], whose Au-dotted $Fe_3O_4$NPs exhibited an XRD pattern dominated by $Fe_3O_4$ peaks.

The morphology of the nanohybrid cellulose microspheres was evaluated by SEM during the sequential stages of the functionalization of the microspheres with the different inorganic NPs. The micrographs displayed in Fig. 5A confirm that the microspheres retained their spherical morphology with dimensions of around 700 μm in the dry state. It should be noted that the different inorganic nanoparticles cannot be observed in the SEM micrographs owing to their small and similar size distribution. Nevertheless, their presence was confirmed by the EDS spectral and mapping data, as mentioned above (Fig. 4A and B). Furthermore, the sequential synthesis of the inorganic nanoparticles originated nanohybrid microspheres with different surface topography, as shown in Fig. 5B.

The surface roughness of Cell/Au–Pt–$Fe_3O_4$NPs was analyzed by AFM. As illustrated in Fig. 5C, the micrograph shows the presence of surface roughness with an average $S_a$ value of 110 nm, which is a somewhat higher than that of unfunctionalized cellulose microspheres (Fig. 3B). The augmentation of the roughness with the inclusion of the inorganic NPs agrees with the SEM micrographs of the microspheres' surface (Fig. 5A and B). Mystek et al. (2020) also described an increase in surface roughness of cellulose beads/spheres with the increasing concentration of cellulose nanocrystals [25]. The nanoscale roughness of the nanohybrid microspheres can play an important role in establishing interactions with organic pollutants, as will be later discussed.

### 3.2.2. *Thermal stability and mechanical performance*

The thermal degradation profile of the nanohybrid cellulose microspheres was assessed by TGA (Fig. 6A). The degradation profile follows a single mass-loss step allocated to the pyrolysis of the regenerated cellulose skeleton [14], alongside the initial dehydration at about 100 °C with a mass loss of ca. 4-5%. The maximum degradation temperature was observed at 325 °C (loss of ca. 39%). At the end of the analysis, the pyrolysis residue accounted for 28%. The Cell/Au–Pt–$Fe_3O_4$NPs nanohybrid exhibits superior thermal properties than, for instance, regenerated cellulose beads modified with activated carbon/$Fe_3O_4$, and activated carbon/$CoFe_2O_4$ [62]. The thermal stability of these nanohybrid cellulose microspheres up to 200-215 °C represents an advantage in industrial applications, where process effluents are often warm or hot, ensuring reliable performance under such conditions.

The mechanical performance of the Cell/Au–Pt–$Fe_3O_4$NPs microspheres was evaluated by nanoindentation and the force-distance curve

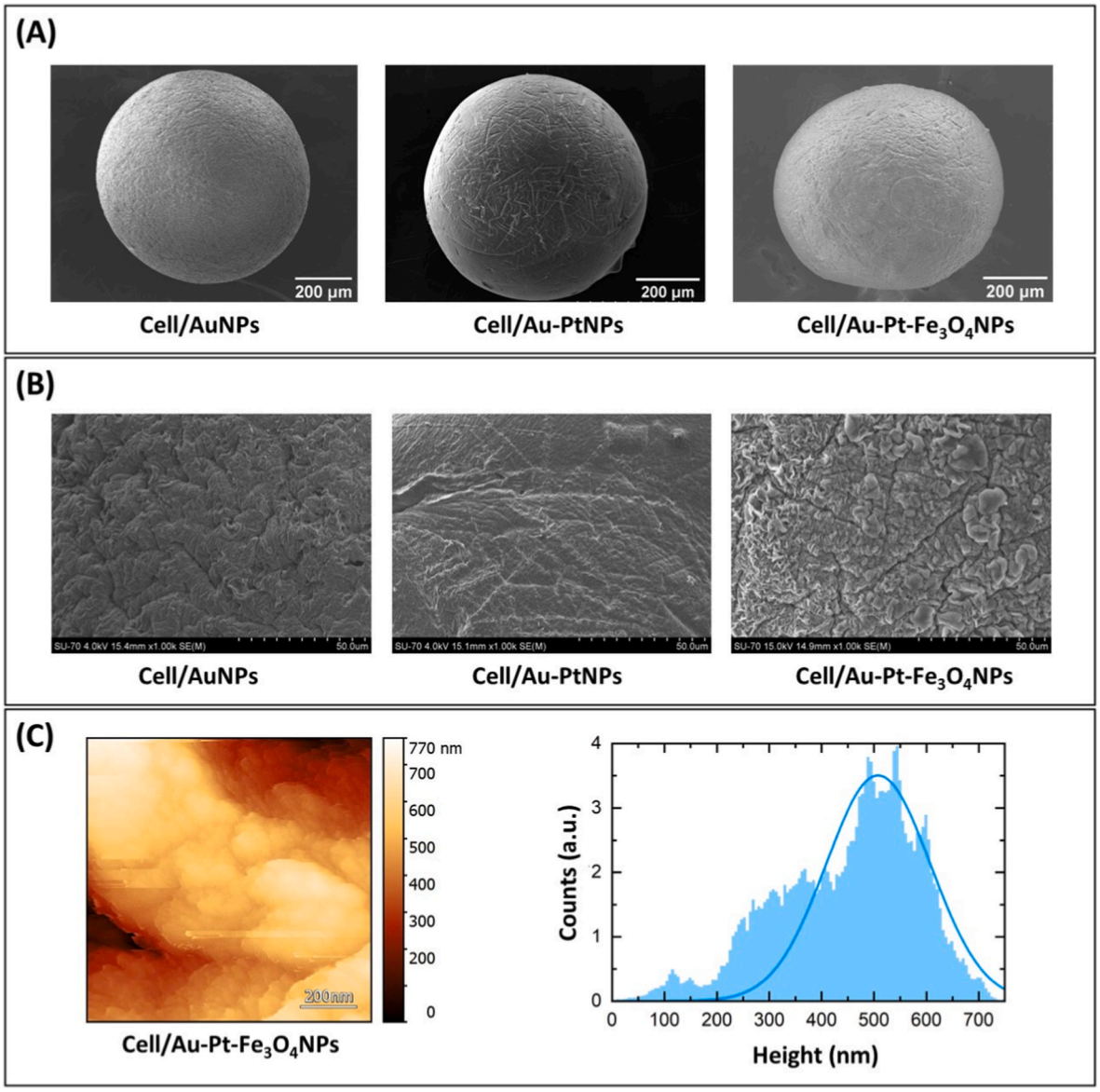


**Fig. 5.** (**A,B**) SEM micrographs with different magnifications of Cell/AuNPs, Cell/Au-PtNPs and Cell/Au–Pt–$Fe_3O_4$NPs, and (**C**) AFM micrograph (left) and roughness analysis (right) of Cell/Au–Pt–$Fe_3O_4$NPs.

measurements are represented in Fig. 6B. The cellulose microspheres functionalized with the three inorganic NPs have Young's modulus values that vary from 1.22 to 2.60 GPa, which are larger than those obtained for the unfunctionalized cellulose microspheres. This indicates that the inclusion of the inorganic nanoparticles increased the elastic modulus of the microspheres, thus rising their stiffness. Conversely, in comparison with the literature, the functionalization of cellulose beads with cellulose nanocrystals at a concentration of 0.5 wt% originated a reduction of the Young's modulus of the ensuing all-cellulose beads relative to the native beads [25].

Overall, the robust Cell/Au–Pt–$Fe_3O_4$NPs nanohybrid microspheres will likely maintain their mechanical integrity during water treatment processes, as will be later demonstrated by the recyclability tests involving consecutive cycles of antibacterial and dye removal assays.

### 3.3. Evaluation of the mobility of the nanohybrid cellulose microspheres

The mobility of the nanohybrid cellulose microspheres was evaluated by performing propulsion tests in an aqueous solution of hydrogen peroxide. The Pt high catalytic activity decomposes $H_2O_2$ into oxygen and water. So, the formation of oxygen bubbles around the Cell/Au–Pt–$Fe_3O_4$NPs microspheres (Fig. 6C) over a 24 h period is a clear evidence of the occurrence of the decomposition reaction of $H_2O_2$ catalyzed by the Pt nanoparticles present on the surface of the microspheres. Therefore, the Cell/Au–Pt–$Fe_3O_4$NPs nanohybrid shows locomotion or propulsion capacity by using $H_2O_2$ as fuel. However, the uniform distribution of the PtNPs on the surface of the nanohybrid cellulose microspheres originates in-place rotation without achieving effective locomotion. The same behavior was observed for the single nanohybrid Cell/PtNPs microspheres (Supplementary Material, Section III.2), as well as the binary nanohybrid Cell/Au-PtNPs microspheres, which suggests that the presence of the AuNPs and $Fe_3O_4$NPs have little or no effect on the catalytic performance of the PtNPs. This is supported by the study of Dong et al. [63], who developed a tailored poly(ε-caprolactone) single crystal coupled with AuNPs, PtNPs and $Fe_3O_4$NPs showing no interference between the catalytic and the non-catalytic components of the hybrid system. Despite the limited movement of the Cell/Au–Pt–$Fe_3O_4$NPs microspheres, the generation of $O_2$-microbubbles might result in enhanced mass transfer and, thus, in improved pollutant removal [64,65].

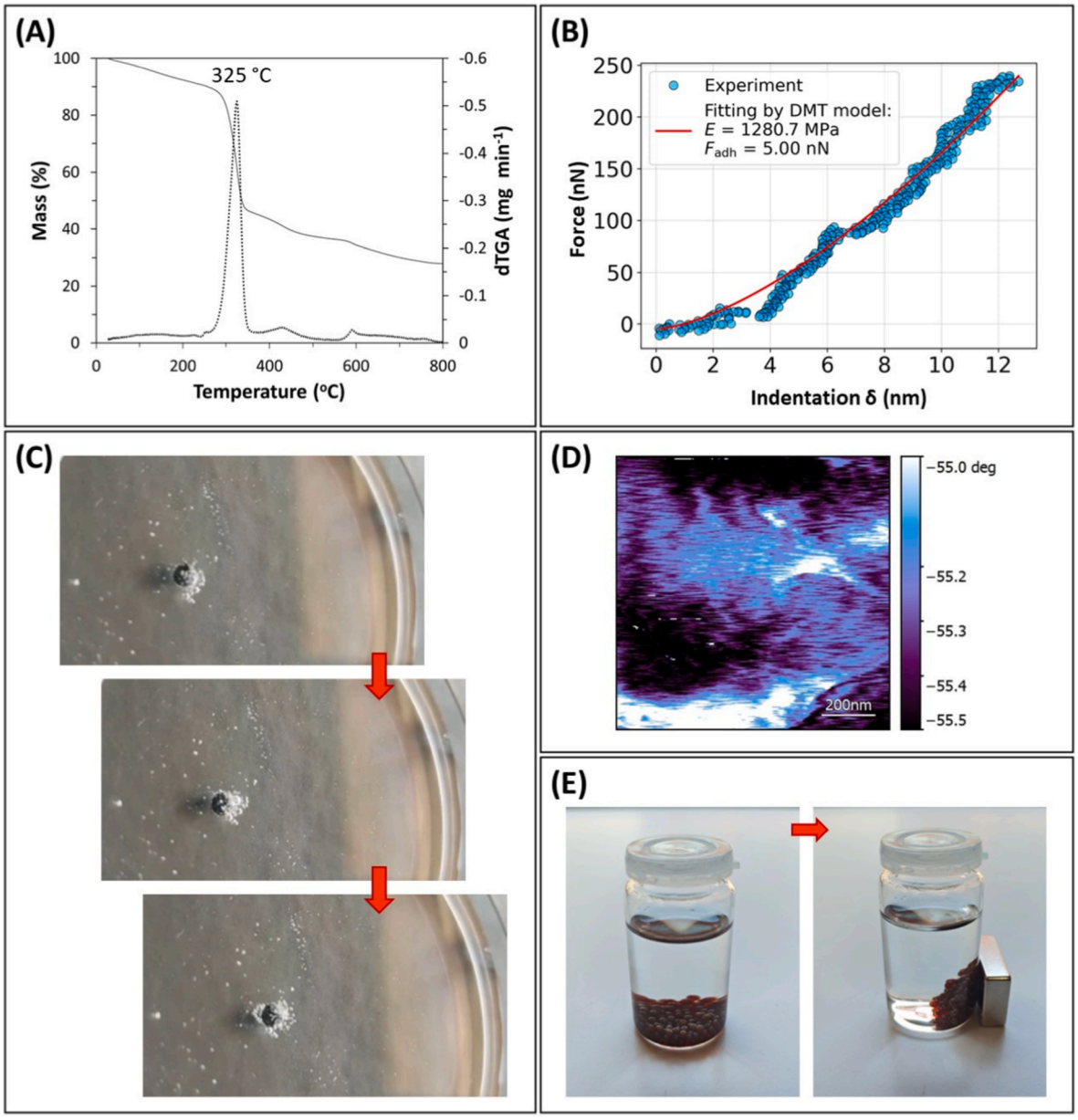


**Fig. 6.** (**A**) TGA thermograms and (**B**) AFM force-indentation depth curve of Cell/Au–Pt–$Fe_3O_4$NPs, (**C**) photographs of the formation of $O_2$-bubbles after placing a Cell/Au–Pt–$Fe_3O_4$NPs microsphere in a Petri dish containing $H_2O_2$ as fuel, (**D**) magnetic force microscopy image of Cell/Au–Pt–$Fe_3O_4$NPs, and (**E**) photographs of the magnetic response of the Cell/Au–Pt–$Fe_3O_4$NPs nanohybrid microspheres before and after exposure to a magnet.

In addition to the catalytic-powered movement, the Cell/Au–Pt–$Fe_3O_4$NPs microspheres can also have a magnetically controlled movement due to the presence of the magnetic $Fe_3O_4$NPs. The magnetic behavior of Cell/Au–Pt–$Fe_3O_4$NPs was studied by MFM. As depicted in Fig. 6D, the phase-contrast variation is very low, which does not allow for a definitive confirmation that the observed contrast arises from magnetic tip-surface interactions rather than from topographic cross-talk. The same result was obtained for the Cell/$Fe_3O_4$NPs single hybrid, as illustrated in Fig. S9B (see Supplementary Material). Although MFM is an elegant technique for examining surface magnetic properties with high resolution and easy sample preparation, it is strongly influenced by the flatness of the surface and the topography of the sample [66]. Nonetheless, the magnetic response was further evaluated by placing the triple functionalized nanohybrid microspheres in contact with a magnet. The images shown in Fig. 6E confirm that the Cell/Au–Pt–$Fe_3O_4$NPs microspheres are capable of a magnetic response in the presence of a magnet.

Overall, the Cell/Au–Pt–$Fe_3O_4$NPs nanohybrid showed a minor locomotion capacity (in-place rotation) due to the catalytic reaction of PtNPs with $H_2O_2$ (Fig. 6C), but a controlled movement owing to the presence of the magnetic $Fe_3O_4$NPs (Fig. 6E). Furthermore, the magnetic properties of the Cell/Au–Pt–$Fe_3O_4$NPs microspheres offer a significant advantage for the envisioned application, as they can be effortlessly separated from water using an external magnet, facilitating easy removal after decontamination. This feature not only enhances operational efficiency but also enables reusability, thus contributing to more cost-effective and sustainable water treatment processes.

### *3.4. In vitro antibacterial activity of the nanohybrid cellulose microspheres*

Gold nanoparticles are known for their antibacterial activity against several bacterial strains, including *Staphylococcus aureus*, *Bacillus subtilis*, *Porphyromonas gingivalis*, *Escherichia coli* and *Pseudomonas aeruginosa*

[67,68]. The mechanism of action of AuNPs is described to be linked with cell lysis and death by electrostatic adsorption on the bacterial surface, membrane damage or reactive oxygen species (ROS) damage to proteins and DNA [68]. This property is particularly relevant in the context of wastewaters, which are typically contaminated with pathogenic microorganisms, including antibiotic-resistant bacteria. Methicillin-resistant *S. aureus* (MRSA) is a representative Gram-positive and clinically challenging pathogen with a significant role in antibacterial resistance, thus posing a major threat to public health. Its selection over Gram-negative bacteria is further related with its prevalence in both urban wastewater [69] and wastewater from healthcare facilities [70], thus making it a suitable and environmentally relevant model for antibacterial studies.

In this sense, the antibacterial activity of the nanohybrid cellulose microspheres (i.e., Cell/Au–Pt–$Fe_3O_4$NPs) was investigated against MRSA. For comparison purposes, the antibacterial activity of the Cell and Cell/AuNPs microspheres was also tested. As anticipated, neither the control nor the regenerated cellulose microspheres (i.e., Cell) hampered the growth of the MRSA pathogenic microorganism, as displayed in Fig. 7A. Even if the content of cellulose microspheres is increased from 5 up to 15 microspheres per assay, this polysaccharide does not have any bactericidal action against MRSA (Fig. 7A). In fact, cellulose lacks any functional groups or moieties that could be responsible for the bacterial inactivation of Gram-positive bacteria such as *S. aureus* [71–73] and *B. subtilis* [74], and Gram-negative bacteria such as *E. coli* [72,73] and *P. aeruginosa* [74], among others.

In contrast, the presence of the AuNPs on the cellulose microspheres lead to a decrease in the initial bacterial concentration. As depicted in Fig. 7B, the Cell/Au–Pt–$Fe_3O_4$NPs nanohybrid exhibited the exact same profile of the nanohybrid containing solely AuNPs (i.e., Cell/AuNPs) reaching reduction values of 1.0-log CFU $mL^{-1}$ after 24 h, 1.4-log CFU $mL^{-1}$ after 48 h and 2.4-log CFU $mL^{-1}$ after 72 h. On one hand, this demonstrates that the nanohybrid cellulose microspheres have bactericidal effect against MRSA. On the other hand, it seems evident that the inclusion of platinum and iron oxide nanoparticles, following the functionalization of cellulose microspheres with AuNPs, neither interfered with the antibacterial inactivation capacity of the AuNPs nor enhanced it. This outcome was anticipated given that AuNPs are a potent agent against MRSA [75], PtNPs can promote the growth of a MRSA biofilm as demonstrated by Jancik-Prochazkova et al. [76], and no inhibitory effect of $Fe_3O_4$NPs on MRSA was reported by Tung et al. [77]. Although the contributions from PtNPs and $Fe_3O_4$NPs cannot be completely excluded, the single nanohybrids Cell/PtNPs and Cell/$Fe_3O_4$NPs did not significantly reduce the initial bacterial concentration of MRSA. Contrarily, the binary nanohybrid Cell/Au-PtNPs displayed a response identical to that of the single (Cell/AuNPs, Fig. 7B) and ternary (Cell/Au–Pt–$Fe_3O_4$NPs, Fig. 7B) nanohybrids, reaching a reduction value of 2.0-log CFU $mL^{-1}$ after 72 h.

As expected, the antibacterial activity of these microspheres is dose-dependent since increasing the content of Cell/Au–Pt–$Fe_3O_4$NPs from 5

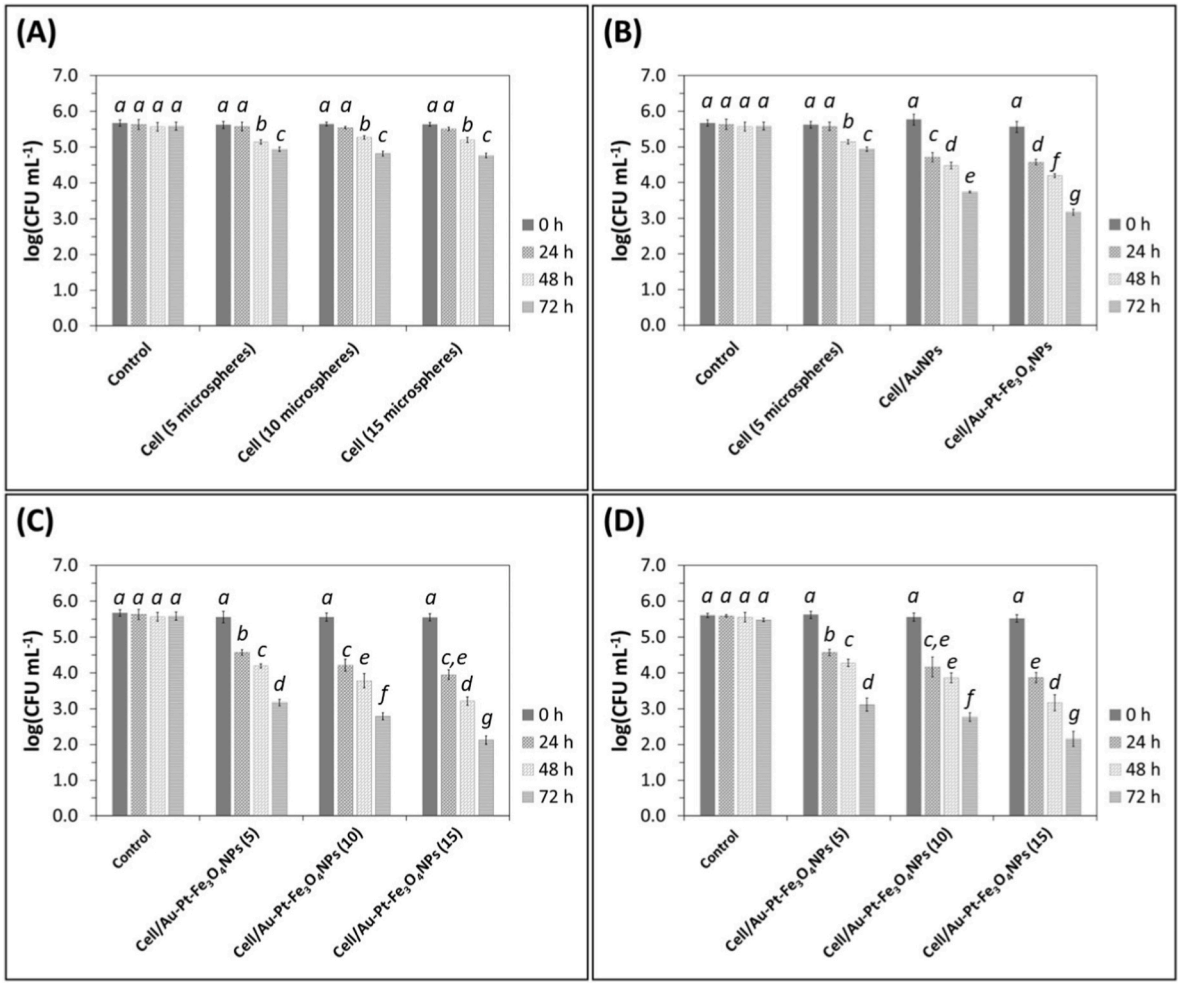


**Fig. 7.** Antibacterial activity assessed at 0, 24, 48 and 72 h for: (**A**) 5, 10 and 15 microspheres of Cell, (**B**) 5 microspheres of Cell, Cell/AuNPs and Cell/Au–Pt–$Fe_3O_4$NPs, (**C**) 5, 10 and 15 microspheres of Cell/Au–Pt–$Fe_3O_4$NPs, and (**D**) 5, 10 and 15 microspheres of reused Cell/Au–Pt–$Fe_3O_4$NPs. Data expressed as means of three independent assays, with error bars indicating standard deviations. Different lower case letters above bars denote statistically significant differences ($p < 0.05$).

to 15 microspheres per assay, generated reduction values in the bacterial concentration of 1.7-log CFU $mL^{-1}$ after 24 h, 2.4-log CFU $mL^{-1}$ after 48 h and 3.4-log CFU $mL^{-1}$ after 72 h.

Following these tests, the microspheres were evaluated for reusability in a second cycle. As shown in Fig. 7D, the Cell/Au–Pt–$Fe_3O_4$NPs nanohybrid microspheres can be reused without a loss of antibacterial activity. In fact, they maintained the same effectiveness as during the initial tests, reaching a maximum value of 3.4-log reduction CFU $mL^{-1}$ after 72 h of contact time with 15 microspheres. This reusable capability is important, as it helps to reduce reliance on single-use materials, even when those materials are derived from renewable raw materials and are potentially biodegradable.

### 3.5. *In vitro aquatic ecotoxicity of the nanohybrid cellulose microspheres*

Given the potential of these nanohybrid cellulose microspheres, their aquatic ecotoxicity was assessed by studying the short-term ecotoxicological effects of water previously exposed to the Cell/Au–Pt–$Fe_3O_4$NPs nanohybrid microspheres, using two distinct model organisms. The freshwater microalga *R. subcapitata* and the non-pathogenic, marine, bioluminescent bacterium *A. fischeri* (formerly *Vibrio fischeri*) were selected for being very sensitive microorganisms to a wide range of toxicants and pollutants [78,79]. This dual-organism approach was chosen to assess the hazardous potential of the nanohybrid cellulose microspheres in freshwater and marine ecosystems.

The algal growth inhibition assay (Fig. 8A) showed no significant reduction in biomass production across all tested concentrations of the water samples previously in contact with the nanohybrid cellulose microspheres. Growth inhibition values ranged from −5.8% to 14.8%, with no clear concentration-dependent response, remaining within the 20% threshold typically associated with experimental variability in toxicity tests [35]. These results suggest that the leachates from the Cell/Au–Pt–$Fe_3O_4$NPs nanohybrid microspheres did not adversely affect algal growth under the tested conditions. Notably, three of the five dilutions exhibited negative inhibition values, indicating that algal growth was stimulated rather than impaired.

Similarly, the bioluminescence inhibition assay using *A. fischeri* (Fig. 8B) revealed no concentration-dependent response after both 15 and 30 min of exposure to the water previously in contact with the Cell/Au–Pt–$Fe_3O_4$NPs nanohybrid microspheres. Inhibition values remained low across all tested concentrations, ranging from 0.0% to 11.2% at 15 min and from −3.1% to 6.3% at 30 min, all within the accepted range of biological variability for *A. fischeri* in toxicity assays. This outcome further supports the conclusion that the Cell/Au–Pt–$Fe_3O_4$NPs nanohybrid microspheres did not release any components or toxic concentrations of components into the water under the experimental conditions tested for the two organisms.

The selection of a marine bacterium as an environmental safety indicator may seem counterintuitive, considering that Cell/Au–Pt–$Fe_3O_4$NPs exhibited antibacterial activity. However, this choice was deliberate, as the primary goal was to generate a material capable of inactivating pathogenic bacterial strains, including antibiotic-resistant bacteria (e.g., MRSA) that threaten human health. By selecting the luminescent bacterium *A. fischeri* as a model organism, the eco-friendliness of the nanohybrid cellulose microspheres was reinforced, ensuring that they do not jeopardize non-pathogenic bacteria involved in supporting nutrient cycling within aquatic ecosystems. However, it is important to note that *A. fischeri* is a Gram-negative model bacterium, which may limit the direct extrapolation of its non-hazardous potential to other non-target bacteria within aquatic environments.

Collectively, these findings offer preliminary evidence of the environmental compatibility of the Cell/Au–Pt–$Fe_3O_4$NPs nanohybrid microspheres. The lack of detectable toxic effects on both freshwater and marine model organisms might suggest that their application in wastewater remediation is unlikely to pose immediate ecotoxicological risks.

### 3.6. *Dye removal tests*

Cellulose microspheres (or cellulose beads) can be used for the removal of inorganic and organic water pollutants, for example, heavy metal ions [59] and organic dyes [62], as reviewed by Hamidon and co-workers [22]. In this sense, the utilization of the Cell/Au–Pt–$Fe_3O_4$NPs microspheres as a biosorbent for the removal of organic dyes, namely methylene blue (MB) and methyl orange (MO), from water samples was evaluated and compared with the microspheres composed solely of regenerated cellulose (i.e., Cell, Fig. 9A and B). MB and MO were selected as model cationic and anionic dyes, respectively, since they are common contaminants in industrial effluents, particularly in the textile industry [80]. These two ionic dyes pose potential health and environmental risks due to their (eco)toxicity [81].

The removal of the organic dyes by the Cell microspheres, which were able to reduce the concentration of MB and MO by 81.3 ± 0.2% and 5.8 ± 0.1% (Fig. 9A), respectively, occurred most likely via adsorption. The attained values are supported by the color intensity of the microspheres after the dye removal test, as illustrated in Fig. 9C. This difference between the two dyes is credited to the selective adsorption capacity of the microspheres towards cationic dyes (viz. MB) due to the hydroxyl groups of cellulose, as reported in the literature for cellulose microspheres with a removal rate of ca. 90% for MB (initial concentration = 50 mg $L^{-1}$, pH = 6.5, time = 180 min) [82].

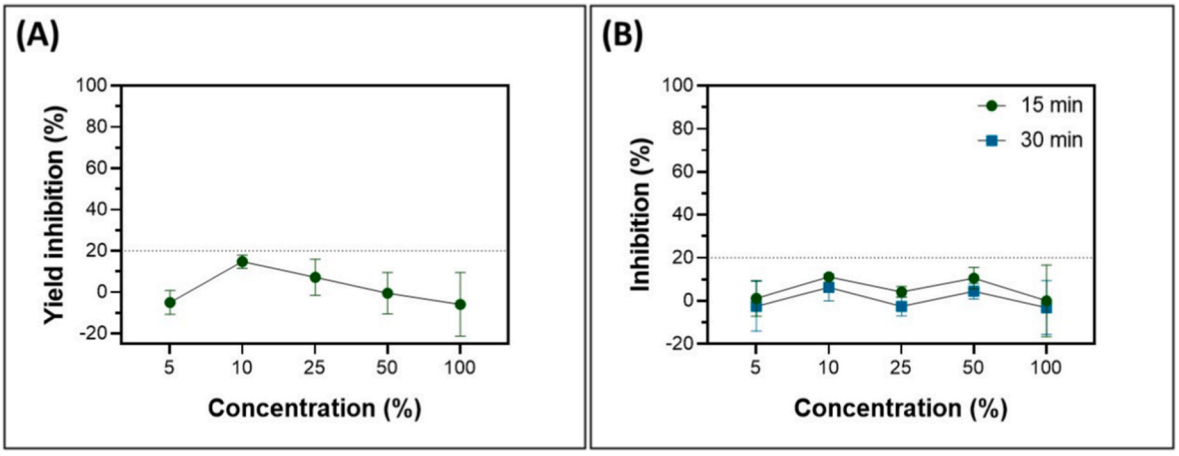


**Fig. 8.** (**A**) Yield Inhibition of *R. subcapitata* after 96 h of exposure to the different concentrations of the water samples previously in contact with Cell/Au–Pt–$Fe_3O_4$NPs, and (**B**) luminescence inhibition of *A. fischeri* after 15 and 30 min of exposure to the different concentrations of the water samples previously in contact with Cell/Au–Pt–$Fe_3O_4$NPs microspheres.

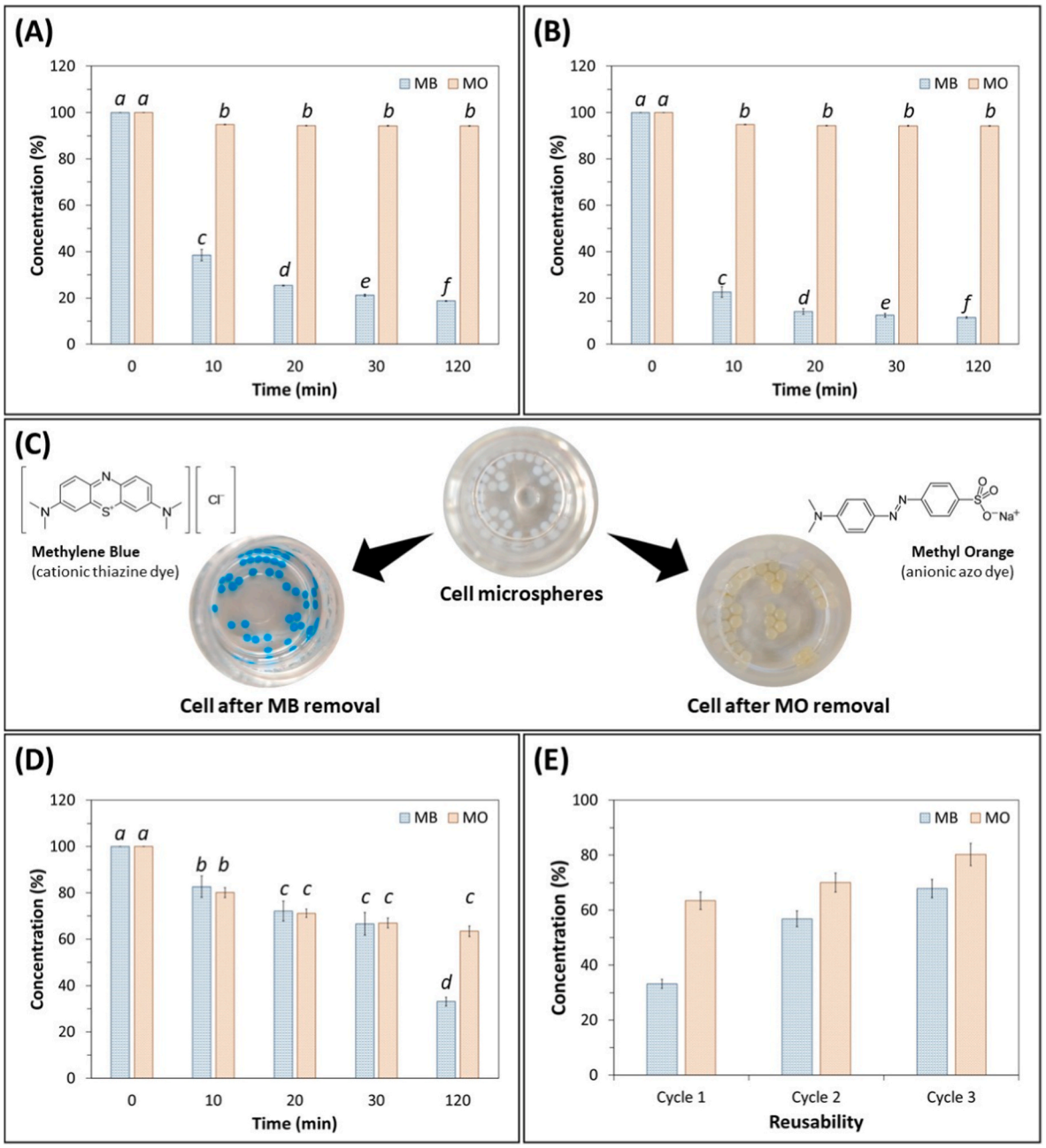


**Fig. 9.** (**A,B**) Removal profile of MB and MO by the cellulose microspheres (i.e., Cell) during 120 min of contact time (**A**) in the absence and (**B**) in the presence of $H_2O_2$; (**C**) photographs of the cellulose microspheres before and after the dye removal, (**D**) removal profile of MB and MO by Cell/Au–Pt–$Fe_3O_4$NPs during 120 min in the presence of $H_2O_2$, and (**E**) reusability of Cell/Au–Pt–$Fe_3O_4$NPs after 3 consecutive cycles of MB and MO removal during 120 min. Different letters denote statistically significant differences ($p < 0.05$).

The removal mechanisms for organic contaminants are either adsorption or degradation processes (e.g., $H_2O_2$-assisted, photocatalytic, or biocatalytic) [83]. Herein, in addition to the well-known adsorption capacity of cellulose, it is important to recognize that the $H_2O_2$ fuel, which will be used to generate $O_2$-bubbles via Pt-catalyzed decomposition, is also a potent oxidizing agent employed in the degradation of organic compounds through $H_2O_2$-assisted oxidation processes [83]. Therefore, the dye removal efficiency of MB and MO using the Cell microspheres was also evaluated in the presence of $H_2O_2$. Fig. 9B shows an 88.4 ± 0.4% reduction in MB concentration after 120 min of contact time, which is higher than the reduction observed without the presence of the oxidizing agent (Fig. 9A). On the contrary, and despite the ability of $H_2O_2$ to disrupt MO molecules through dissociation, this oxidant is stable in the presence of this organic dye, requiring the use of catalysts or radiation to activate the oxidizing agent and expedite the reaction [84]. Therefore, the values for MO remained unchanged compared to those in the absence of $H_2O_2$ (Fig. 9A).

Regarding the Cell/Au–Pt–$Fe_3O_4$NPs microspheres, the dye removal tests were all performed in the presence of $H_2O_2$. In this case, the color of the dark nanohybrid microspheres cannot be used as the first proof for confirming the removal of either dyes. In accordance with Fig. 9D, the nanohybrid microspheres were capable of reducing the concentration of MB and MO by 66.8 ± 1.9% and 36.7 ± 2.4%, respectively, after 120 min of contact time.

Compared with the unfunctionalized microspheres (Fig. 9B), these results point out an inferior removal performance of the nanohybrid microspheres for the cationic dye (MB), but demonstrated a superior capacity for removing the anionic dye (MO). This difference can be

ascribed to the distinct constituents of the nanohybrid microspheres, which influence their surface properties and, consequently, affect the accessibility and availability of adsorption sites [22]. Additionally, it is important to note the $Fe_3O_4$NPs are known for being effective heterogeneous catalysts for Fenton-like reactions that use $H_2O_2$ as an oxidant to facilitate the degradation of organic compounds [85].

In relation to existing studies, Cell/Au–Pt–$Fe_3O_4$NPs exhibit a lower removal efficiency than, for instance, the cellulose-alginate core-shell microspheres with a removal rate of 99.98% of MB (initial concentration = 50 mg $L^{-1}$, pH = 6.5, time = 180 min) [82].

Lastly, the Cell/Au–Pt–$Fe_3O_4$NPs nanohybrid microspheres were evaluated for reusability in a second and third cycles of dye removal. According to Fig. 9E, the hybrid microspheres lost some of their removal efficiency cycle after cycle. In fact, the Cell/Au–Pt–$Fe_3O_4$NPs reduced the concentrations of MB and MO by 43.1 ± 2.7% and 29.9 ± 2.8%, respectively, after 120 min of contact during the second cycle. In the third cycle, they achieved reductions of 32.1 ± 1.9% for MB and 19.7 ± 2.5% for MO under the same conditions (Fig. 9E). The EDS analysis of the Cell/Au–Pt–$Fe_3O_4$NPs nanohybrid after the third cycle of dye removal (of both MB and MO) showed a normalized elemental composition (wt.%) of about 20% C, 40% O, 1% Au, 2% Pt, and 37% Fe. This surface composition is similar to that of the initial nanohybrid cellulose microspheres, which indicates that the inorganic NPs did not leach during the dye removal tests. Therefore, the observed decrease in dye removal efficiency after repeated use is likely due to surface blockage rather than NPs leaching. Although the removal efficiency decreases after 3 consecutive cycles, the reusable capability remains significant and higher than that obtained with the Cell microspheres for the case of the anionic dye (MO).

All-inclusive, these non-ecotoxic nanohybrid cellulose microspheres have the ability to effectively kill antibiotic-resistant bacteria and remove toxic organic dyes, with the added convenience of easy recovery via an external magnetic field and reusability for lowering production costs. Besides, they can contribute to reducing the dependence on single-use materials, even when such materials are sourced from renewable raw materials and are potentially biodegradable.

## 4. Conclusions

Cellulose hybrid microspheres were successfully fabricated via dissolution of wood pulp fibers in an organic electrolyte solution, followed by regeneration in water, and functionalization with inorganic nanoparticles. The Cell/Au–Pt–$Fe_3O_4$NPs nanohybrid microspheres, with a diameter of 2.3 ± 0.5 mm in the wet state and 680 ± 5 μm after drying, showed a content of 207 ± 5 μg $g^{-1}$ of Au, 649 ± 64 μg $g^{-1}$ of Pt and 59.7 ± 0.6 mg $g^{-1}$ of Fe. Moreover, they have a catalytic-powered and magnetically controlled movement due to the presence of the catalytic PtNPs and the magnetic $Fe_3O_4$NPs, respectively. The Cell/Au–Pt–$Fe_3O_4$NPs nanohybrid microspheres showed antibacterial activity against the pathogenic bacterium MRSA, as supported by the 3.4-log CFU $mL^{-1}$ reduction of its concentration. In addition, the nanohybrid cellulose microspheres were able to degrade two water-soluble model dyes, reducing the MB concentration by ca. 67% and the MO concentration by ca. 37%, with the possibility of being reused up to 3-cycles. Furthermore, the nanohybrid cellulose microspheres showed to be environmentally safe to aquatic biota as supported by the lack of toxicity towards the microalgae *R. subcapitata* and the non-pathogenic marine bacterium *A. fischeri*.

Overall, the results demonstrate that the nanohybrid cellulose microspheres incorporating three different inorganic nanoparticles (AuNPs, PtNPs and $Fe_3O_4$NPs) can effectively move and treat water contaminated with pathogenic bacteria and organic pollutants, with apparently good environmental friendliness levels. Furthermore, their magnetic properties facilitate ease recovery through an external magnetic field, which significantly improves their practicality and potential for real-world applications.

## CRediT authorship contribution statement

**Joana C. Almeida:** Investigation, Methodology, Writing – original draft, Writing – review & editing. **William M. Facchinatto:** Investigation, Methodology, Writing – review & editing. **Vasco Valente:** Investigation, Methodology, Writing – review & editing. **Gabriela J. Campos:** Investigation, Writing – review & editing. **Denis Alikin:** Investigation, Methodology, Writing – review & editing. **Andrei Kholkin:** Funding acquisition, Resources, Writing – review & editing. **Nicolas Schaeffer:** Investigation, Methodology, Writing – review & editing. **Armando J.D. Silvestre:** Funding acquisition, Resources, Writing – review & editing. **Fátima Jesus:** Investigation, Methodology, Writing – review & editing. **Joana L. Pereira:** Funding acquisition, Investigation, Methodology, Resources, Writing – review & editing. **Adelaide Almeida:** Funding acquisition, Resources, Writing – review & editing. **Carmen S.R. Freire:** Conceptualization, Funding acquisition, Resources, Writing – review & editing. **Carla Vilela:** Conceptualization, Funding acquisition, Methodology, Project administration, Resources, Supervision, Writing – original draft, Writing – review & editing.

## Declaration of competing interest

The authors declare that they have no known competing financial interests or personal relationships that could have appeared to influence the work reported in this paper.

## Acknowledgments

This work was developed within the scope of the projects CICECO – Aveiro Institute of Materials, UID/50011/2025 (DOI 10.54499/UID/50011/2025) & LA/P/0006/2020 (DOI 10.54499/LA/P/0006/2020) & UID/PRR/50011/2025 (DOI 10.54499/UID/PRR/50011/2025), and CESAM – Centre for Environmental and Marine Studies, UID/50017/2025 (doi.org/10.54499/UID/50017/2025) and LA/P/0094/2020 (DOI 10.54499/LA/P/0094/2020), financed by national funds through the FCT/MCTES (PIDDAC), and project Cell4Janus: Engineering self-propelled cellulose-based Janus microrobots (DOI 10.54499/PTDC/BII-BIO/1901/2021), financially supported by national funds (OE), through FCT/MCTES. FCT is also acknowledged for the research contracts under Scientific Employment Stimulus to D.A. (DOI 10.54499/2023.09305. CEECIND/CP2840/CT0020) and C.V. (DOI 10.54499/2021.01571. CEECIND/CP1659/CT0024). A.K. thanks the ERA-Chair project "FeLow-D" funded by the European Union's HORIZON-WIDERA-2023-TALENTS-01 Horizon 2020 research and innovation program under Grant Agreement ID 101186499 (DOI 10.3030/101186499).

## Appendix A. Supplementary data

Supplementary data to this article can be found online at https://doi.org/10.1016/j.mtchem.2026.103801.

## Data availability

Data will be made available on request.

## References

[1] K. Heise, E. Kontturi, Y. Allahverdiyeva, T. Tammelin, M.B. Linder, Nonappa, O. Ikkala, Nanocellulose: recent fundamental advances and emerging biological and biomimicking applications, Adv. Mater. 33 (2020) 2004349, https://doi.org/10.1002/adma.202004349.

[2] T. Li, C. Chen, A.H. Brozena, J.Y. Zhu, L. Xu, C. Driemeier, J. Dai, O.J. Rojas, A. Isogai, L. Wågberg, L. Hu, Developing fibrillated cellulose as a sustainable technological material, Nature 590 (2021) 47–56, https://doi.org/10.1038/s41586-020-03167-7.

[3] D. Klemm, E.D. Cranston, D. Fischer, M. Gama, S.A. Kedzior, D. Kralisch, F. Kramer, T. Kondo, T. Lindström, S. Nietzsche, K. Petzold-Welcke, F. Rauchfuß,

Nanocellulose as a natural source for groundbreaking applications in materials science: today's state, Mater. Today 21 (2018) 720–748, https://doi.org/10.1016/j.mattod.2018.02.001.
[4] B. Thomas, M.C. Raj, A.K. B, R.M. H, J. Joy, A. Moores, G.L. Drisko, C. Sanchez, Nanocellulose, a versatile green platform: from biosources to materials and their applications, Chem. Rev. 118 (2018) 11575–11625, https://doi.org/10.1021/acs.chemrev.7b00627.
[5] K. Jedvert, T. Heinze, Cellulose modification and shaping - a review, J. Polym. Eng. 37 (2017) 845–860, https://doi.org/10.1515/polyeng-2016-0272.
[6] M.T. Clough, K. Geyer, P.A. Hunt, S. Son, U. Vagt, T. Welton, Ionic liquids: not always innocent solvents for cellulose, Green Chem. 17 (2015) 231–243, https://doi.org/10.1039/c4gc01955e.
[7] B. Azimi, H. Maleki, V. Gigante, R. Bagherzadeh, A. Mezzetta, M. Milazzo, L. Guazzelli, P. Cinelli, A. Lazzeri, S. Danti, Cellulose-based fiber spinning processes using ionic liquids, Cellulose 29 (2022) 3079–3129, https://doi.org/10.1007/s10570-022-04473-1.
[8] H. Fu, X. Wang, H. Sang, Y. Hou, X. Chen, X. Feng, Dissolution behavior of microcrystalline cellulose in DBU-based deep eutectic solvents: insights from spectroscopic investigation and quantum chemical calculations, J. Mol. Liq. 299 (2020) 112140, https://doi.org/10.1016/j.molliq.2019.112140.
[9] S. Alsoy Altinkaya, A perspective on cellulose dissolution with deep eutectic solvents, Front. Membr. Sci. Technol. 3 (2024) 1382054, https://doi.org/10.3389/frmst.2024.1382054.
[10] R. Rinaldi, Instantaneous dissolution of cellulose in organic electrolyte solutions, Chem. Commun. 47 (2011) 511–513, https://doi.org/10.1039/c0cc02421j.
[11] E. Gale, R.H. Wirawan, R.L. Silveira, C.S. Pereira, M.A. Johns, M.S. Skaf, J.L. Scott, Directed discovery of greener cosolvents: new cosolvents for use in ionic liquid based organic electrolyte solutions for cellulose dissolution, ACS Sustain. Chem. Eng. 4 (2016) 6200–6207, https://doi.org/10.1021/acssuschemeng.6b02020.
[12] M.T. Clough, Organic electrolyte solutions as versatile media for the dissolution and regeneration of cellulose, Green Chem. 19 (2017) 4754–4768, https://doi.org/10.1039/c7gc01776f.
[13] S.T. Kim, S. Cho, M. Song, S.T. Chang, Microfluidic synthesis of microfibers based on regeneration of cellulose from ionic liquids, Polymer 39 (2015) 588–592, https://doi.org/10.7317/pk.2015.39.4.588.
[14] B. Pereira, F.S. Matos, B.F.A. Valente, N. Von Weymarn, T. Kamppuri, C.S.R. Freire, A.J.D. Silvestre, C. Vilela, From regenerated wood pulp fibers to cationic cellulose: preparation, characterization and dyeing properties, Polysaccharides 3 (2022) 609–624, https://doi.org/10.3390/polysaccharides3030036.
[15] F.S. Matos, S. Fateixa, N. von Weymarn, C.S.R. Freire, A.J.D. Silvestre, C. Vilela, Functional fibers from regenerated wood pulp cellulose and a natural-based phytate with enhanced flame retardancy properties, J. Appl. Polym. Sci. 140 (2023) e54326, https://doi.org/10.1002/app.54326.
[16] J. Shuai, X. Gao, J. Zhao, W. Ge, M. Tian, Z. Lei, X. Wang, Dissolution and regeneration of cellulose using superbase-based dicarboxylic ionic liquids with tailored amphiphilicity, Chem. Eng. J. 495 (2024) 153280, https://doi.org/10.1016/j.cej.2024.153280.
[17] K. Huang, Y. Wang, Recent applications of regenerated cellulose films and hydrogels in food packaging, Curr. Opin. Food Sci. 43 (2022) 7–17, https://doi.org/10.1016/j.cofs.2021.09.003.
[18] J.P.F. Carvalho, A.C.Q. Silva, A.J.D. Silvestre, C.S.R. Freire, C. Vilela, Spherical cellulose micro and nanoparticles: a review of recent developments and applications, Nanomaterials 11 (2021) 2744, https://doi.org/10.3390/nano11102744.
[19] B. El Allaoui, H. Benzeid, N. Zari, A. el kacem Qaiss, R. Bouhfid, Functional cellulose-based beads for drug delivery: preparation, functionalization, and applications, J. Drug Deliv. Sci. Technol. 88 (2023) 104899, https://doi.org/10.1016/j.jddst.2023.104899.
[20] Cellufine$^{tm}$, 2021. https://www.jnc-corp.co.jp/fine/en/cellufine/. (Accessed 28 April 2026).
[21] Macroporous Bead Cellulose MT, 2021. https://www.iontosorb.cz/pages/bead.htm. (Accessed 28 April 2026).
[22] T.S. Hamidon, R. Adnan, M.K.M. Haafiz, M.H. Hussin, Cellulose-based beads for the adsorptive removal of wastewater effluents: a review, Environ. Chem. Lett. 20 (2022) 1965–2017, https://doi.org/10.1007/s10311-022-01401-4.
[23] G. Bayramoglu, S. Tilki, M.Y. Arica, Preparation of amine or carboxyl groups modified cellulose beads for removal of uranium (VI) ions from aqueous solutions, Cellulose 31 (2024) 5133–5149, https://doi.org/10.1007/s10570-024-05909-6.
[24] R.M.P. Karlsson, P.T. Larsson, S. Yu, S.A. Pendergraph, T. Pettersson, J. Hellwig, L. Wågberg, Carbohydrate gel beads as model probes for quantifying non-ionic and ionic contributions behind the swelling of delignified plant fibers, J. Colloid Interface Sci. 519 (2018) 119–129, https://doi.org/10.1016/j.jcis.2018.02.052.
[25] K. Mystek, M.S. Reid, P.A. Larsson, L. Wågberg, In situ modification of regenerated cellulose beads: creating all-cellulose composites, Ind. Eng. Chem. Res. 59 (2020) 2968–2976, https://doi.org/10.1021/acs.iecr.9b06273.
[26] A.A. Altam, L. Zhu, W. Huang, H. Huang, S. Yang, Polyelectrolyte complex beads of carboxymethylcellulose and chitosan: the controlled formation and improved properties, Carbohydr. Polym. Technol. Appl. 2 (2021) 100100, https://doi.org/10.1016/j.carpta.2021.100100.
[27] M.M.H. Rocky, I.M.M. Rahman, F.B. Biswas, S. Rahman, M. Endo, K.H. Wong, A. S. Mashio, H. Hasegawa, Cellulose-based materials for scavenging toxic and precious metals from water and wastewater: a review, Chem. Eng. J. 472 (2023) 144677, https://doi.org/10.1016/j.cej.2023.144677.
[28] A. Etale, A.J. Onyianta, S.R. Turner, S.J. Eichhorn, Cellulose: a review of water interactions, applications in composites, and water treatment, Chem. Rev. 123 (2023) 2016–2048, https://doi.org/10.1021/acs.chemrev.2c00477.
[29] A. Darmenbayeva, R. Rajasekharan, B. Massalimova, N. Bektenov, R. Taubayeva, K. Bazarbaeva, M. Kurmanaliev, Z. Mukazhanova, A. Nurlybayeva, K. Bulekbayeva, A. Kabylbekova, A. Ungarbayeva, Cellulose-based sorbents: a comprehensive review of current advances in water remediation and future prospects, Molecules 29 (2024) 5969, https://doi.org/10.3390/molecules29245969.
[30] J. Yu, A.C. Wang, M. Zhang, Z. Lin, Water treatment via non-membrane inorganic nanoparticles/cellulose composites, Mater. Today 50 (2021) 329–357, https://doi.org/10.1016/j.mattod.2021.03.024.
[31] R.J.B. Pinto, D. Bispo, C. Vilela, A.M.P. Botas, R.A.S. Ferrreira, A.C. Menezes, F. Campos, H. Oliveira, M.H. Abreu, S.A.O. Santos, C.S.R. Freire, One-minute synthesis of size-controlled fucoidan-gold nanosystems: antitumoral activity and dark field imaging, Materials 13 (2020) 1076, https://doi.org/10.3390/ma13051076.
[32] W. Wu, S.-B. He, H.-P. Peng, H.-H. Deng, A.-L. Liu, X.-H. Lin, X.-H. Xia, W. Chen, Citrate-capped platinum nanoparticle as a smart probe for ultrasensitive mercury sensing, Anal. Chem. 86 (2014) 10955–10960, https://doi.org/10.1021/ac503544w.
[33] I. Alfaro, L. Molina, P. González, J. Gaete, F. Valenzuela, J.F. Marco, C. Sáez, C. Basualto, Silica-coated magnetite nanoparticles functionalized with betaine and their use as an adsorbent for Mo(VI) and Re(VII) species from acidic aqueous solutions, J. Ind. Eng. Chem. 78 (2019) 271–283, https://doi.org/10.1016/j.jiec.2019.06.002.
[34] J. Lübbe, L. Doering, M. Reichling, Precise determination of force microscopy cantilever stiffness from dimensions and eigenfrequencies, Meas. Sci. Technol. 23 (2012) 045401, https://doi.org/10.1088/0957-0233/23/4/045401.
[35] OECD, Test No. 201: Freshwater Alga and Cyanobacteria, Growth Inhibition Test, OECD Guidel. Test. Chem. (2011), https://doi.org/10.1787/9789264070561-en. https://doi.org/10.1787/9789264069923-en. Paris.
[36] S.W. Geis, K.L. Fleming, E.T. Korthals, G. Searle, L. Reynolds, D.A. Karner, Modifications to the algal growth inhibition test for use as a regulatory assay, Environ. Toxicol. Chem. 19 (2000) 36–41, https://doi.org/10.1002/etc.5620190105.
[37] J.R. Stein, Handbook of Phycological Methods: Culture Methods and Growth Measurements, Cambridge University Press, Cambridg, 1979.
[38] A. Magdeburg, D. Stalter, J. Oehlmann, Whole effluent toxicity assessment at a wastewater treatment plant upgraded with a full-scale post-ozonation using aquatic key species, Chemosphere 88 (2012) 1008–1014, https://doi.org/10.1016/j.chemosphere.2012.04.017.
[39] A. Tolba, M. Gar Alalm, M. Elsamadony, A. Mostafa, H. Afify, D.D. Dionysiou, Modeling and optimization of heterogeneous Fenton-like and photo-Fenton processes using reusable $Fe_3O_4$-MWCNTs, Process Saf. Environ. Prot. 128 (2019) 273–283, https://doi.org/10.1016/j.psep.2019.06.011.
[40] D. Klemm, B. Heublein, H.-P. Fink, A. Bohn, Cellulose: fascinating biopolymer and sustainable raw material, Angew. Chem. Int. Ed. 44 (2005) 3358–3393, https://doi.org/10.1002/anie.200460587.
[41] L. Lei, A. Lindbråthen, M. Sandru, M.T.G. Gutierrez, X. Zhang, M. Hillestad, X. He, Spinning cellulose hollow fibers using 1-ethyl-3-methylimidazolium acetate–dimethylsulfoxide Co-Solvent, Polymers 10 (2018) 972, https://doi.org/10.3390/polym10090972.
[42] X. Tan, X. Li, L. Chen, F. Xie, Solubility of starch and microcrystalline cellulose in 1-ethyl-3-methylimidazolium acetate ionic liquid and solution rheological properties, Phys. Chem. Chem. Phys. 18 (2016) 27584–27593, https://doi.org/10.1039/c6cp04426c.
[43] F. Lu, J. Song, B.W. Cheng, X.J. Ji, L.J. Wang, Viscoelasticity and rheology in the regimes from dilute to concentrated in cellulose 1-ethyl-3-methylimidazolium acetate solutions, Cellulose 20 (2013) 1343–1352, https://doi.org/10.1007/S10570-013-9885-7/FIGURES/8.
[44] X. Tan, L. Chen, X. Li, F. Xie, Effect of anti-solvents on the characteristics of regenerated cellulose from 1-ethyl-3-methylimidazolium acetate ionic liquid, Int. J. Biol. Macromol. 124 (2019) 314–320, https://doi.org/10.1016/j.ijbiomac.2018.11.138.
[45] H. Li, K. Mystek, L. Wågberg, T. Pettersson, Development of mechanical properties of regenerated cellulose beads during drying as investigated by atomic force microscopy, Soft Matter 16 (2020) 6457–6462, https://doi.org/10.1039/d0sm00866d.
[46] E.J. Foster, R.J. Moon, U.P. Agarwal, M.J. Bortner, J. Bras, S. Camarero-Espinosa, K.J. Chan, M.J.D. Clift, E.D. Cranston, S.J. Eichhorn, D.M. Fox, W.Y. Hamad, L. Heux, B. Jean, M. Korey, W. Nieh, K.J. Ong, M.S. Reid, S. Renneckar, R. Roberts, J.A. Shatkin, J. Simonsen, K. Stinson-Bagby, N. Wanasekara, J. Youngblood, Current characterization methods for cellulose nanomaterials, Chem. Soc. Rev. 47 (2018) 2609–2679, https://doi.org/10.1039/c6cs00895j.
[47] F. Xu, B.U. Cho, Preparation of porous regenerated cellulose microstructures via emulsion-coagulation technique, Cellulose 29 (2022) 1527–1542, https://doi.org/10.1007/s10570-022-04428-6.
[48] S. Elsayed, M. Hummel, D. Sawada, C. Guizani, M. Rissanen, H. Sixta, Superbase-based protic ionic liquids for cellulose filament spinning, Cellulose 28 (2021) 533–547, https://doi.org/10.1007/s10570-020-03505-y.
[49] K.N. Onwukamike, T. Tassaing, S. Grelier, E. Grau, H. Cramail, M.A.R. Meier, Detailed understanding of the DBU/$CO_2$ switchable solvent system for cellulose solubilization and derivatization, ACS Sustain. Chem. Eng. 6 (2018) 1496–1503, https://doi.org/10.1021/acssuschemeng.7b04053.
[50] J.-H. Pang, X. Liu, M. Wu, Y.-Y. Wu, X.-M. Zhang, R.-C. Sun, Fabrication and characterization of regenerated cellulose films using different ionic liquids, J. Spectrosc. (2014) 214057, https://doi.org/10.1155/2014/214057.
[51] J. Pang, M. Wu, Q. Zhang, X. Tan, F. Xu, X. Zhang, R. Sun, Comparison of physical properties of regenerated cellulose films fabricated with different cellulose

feedstocks in ionic liquid, Carbohydr. Polym. 121 (2015) 71–78, https://doi.org/10.1016/J.CARBPOL.2014.11.067.
[52] T.D.O. Gadim, C. Vilela, F.J.A. Loureiro, A.J.D. Silvestre, C.S.R. Freire, F.M. L. Figueiredo, Nafion® and nanocellulose: a partnership for greener polymer electrolyte membranes, Ind. Crops Prod. 93 (2016) 212–218, https://doi.org/10.1016/j.indcrop.2016.01.028.
[53] H. Li, M. Kruteva, K. Mystek, M. Dulle, W. Ji, T. Pettersson, L. Wågberg, Macro- and microstructural evolution during drying of regenerated cellulose beads, ACS Nano 14 (2020) 6774–6784, https://doi.org/10.1021/acsnano.0c00171.
[54] H. Li, M. Kruteva, M. Dulle, Z. Wang, K. Mystek, W. Ji, T. Pettersson, L. Wågberg, Understanding the drying behavior of regenerated cellulose gel beads: the effects of concentration and nonsolvents, ACS Nano 16 (2022) 2608–2620, https://doi.org/10.1021/acsnano.1c09338.
[55] J. Wu, M.P. Andrews, Mechanical, morphological and comparative properties of microbeads assembled from carboxylated cellulose nanocrystals, J. Mater. Chem. A 12 (2023) 950–960, https://doi.org/10.1039/d3ta05298b.
[56] C. Vilela, A.C.Q. Silva, E.M. Domingues, G. Gonçalves, M.A. Martins, F.M. L. Figueiredo, S.A.O. Santos, C.S.R. Freire, Conductive polysaccharides-based proton-exchange membranes for fuel cell applications: the case of bacterial cellulose and fucoidan, Carbohydr. Polym. 230 (2020) 115604, https://doi.org/10.1016/j.carbpol.2019.115604.
[57] P. Anbu, S.C.B. Gopinath, S. Jayanthi, Synthesis of gold nanoparticles using Platycodon grandiflorum extract and its antipathogenic activity under optimal conditions, Nanomater. Nanotechnol. 10 (2020) 1–9, https://doi.org/10.1177/1847980420961697.
[58] S. Lee, C. Yim, S. Jeon, Direct synthesis of platinum nanodots in ZIF-8/$Fe_3O_4$ core-shell hybrid nanoparticles, RSC Adv. 7 (2017) 31239–31243, https://doi.org/10.1039/c7ra04711h.
[59] X. Luo, X. Lei, N. Cai, X. Xie, Y. Xue, F. Yu, Removal of heavy metal ions from water by magnetic cellulose- based beads with embedded chemically modified magnetite nanoparticles and activated carbon, ACS Sustain. Chem. Eng. 4 (2016) 3960–3969, https://doi.org/10.1021/acssuschemeng.6b00790.
[60] N. Yadav, A.K. Jaiswal, K.K. Dey, V.B. Yadav, G. Nath, A.K. Srivastava, R.R. Yadav, Trimetallic Au/Pt/Ag based nanofluid for enhanced antibacterial response, Mater. Chem. Phys. 218 (2018) 10–17, https://doi.org/10.1016/j.matchemphys.2018.07.016.
[61] E.C.H.T. Lau, M. Åhlén, O. Cheung, A.Y. Ganin, D.G.E. Smith, H.H.P. Yiu, Gold-iron oxide (Au/$Fe_3O_4$) magnetic nanoparticles as the nanoplatform for binding of bioactive molecules through self-assembly, Front. Mol. Biosci. 10 (2023) 1143190, https://doi.org/10.3389/fmolb.2023.1143190.
[62] S. Moosavi, S. Gan, S. Zakaria, Functionalized cellulose beads with activated carbon $Fe_3O_4$/$CoFe_2O_4$ for cationic dye removal, Cellul. Chem. Technol. 53 (2019) 815–825, https://doi.org/10.35812/CelluloseChemTechnol.2019.53.80.
[63] B. Dong, T. Zhou, H. Zhang, C.Y. Li, Directed self-assembly of nanoparticles for nanomotors, ACS Nano 7 (2013) 5192–5198, https://doi.org/10.1021/nn400925q.
[64] B. Jurado-Sánchez, J. Wang, Micromotors for environmental applications: a review, Environ. Sci. Nano 5 (2018) 1530–1544, https://doi.org/10.1039/C8EN00299A.
[65] M. Yew, Y. Ren, K.S. Koh, C. Sun, C. Snape, A review of state-of-the-art microfluidic technologies for environmental applications: detection and remediation, Glob. Chall. 3 (2019) 1800060, https://doi.org/10.1002/gch2.201800060.
[66] J. Impundu, S. Hussain, E. Minani, H. Liu, Y.J. Li, L. Sun, Local magnetic characterization of 1D and 2D carbon nanomaterials with magnetic force microscopy techniques: a review, Mater. Today Commun. 35 (2023) 106103, https://doi.org/10.1016/j.mtcomm.2023.106103.
[67] E.K. Tian, Y. Wang, R. Ren, W. Zheng, W. Liao, Gold nanoparticle: recent progress on its antibacterial applications and mechanisms, J. Nanomater. (2021) 2501345, https://doi.org/10.1155/2021/2501345.
[68] X. Gu, Z. Xu, L. Gu, H. Xu, F. Han, B. Chen, X. Pan, Preparation and antibacterial properties of gold nanoparticles: a review, Environ. Chem. Lett. 19 (2021) 167–187, https://doi.org/10.1007/s10311-020-01071-0.
[69] A.I. Al-Mustapha, A. Tiwari, V. Johansson, V. Heljanko, L. Kirsi-Maarit, A. Lipponen, S. Oikarinen, T. Pitkänen, A. Heikinheimo, Characterization of methicillin resistant Staphylococcus aureus in municipal wastewater in Finland, One Health 19 (2024) 100881, https://doi.org/10.1016/j.onehlt.2024.100881.
[70] A.O. Adekanmbi, R.O. Adesola, A.O. Adeyemi, C.C. Mbionwu, The threat of methicillin resistant Staphylococcus aureus (MRSA) in the aquatic environment via wastewater generated from healthcare facilities, in: K. Garbacz, T. Jarzembowski (Eds.), Bact. Infect. Dis., IntechOpen, 2023, https://doi.org/10.5772/intechopen.113967.
[71] D.F.S. Fonseca, J.P.F. Carvalho, V. Bastos, H. Oliveira, C. Moreirinha, A. Almeida, A.J.D. Silvestre, C. Vilela, C.S.R. Freire, Antibacterial multi-layered nanocellulose-based patches loaded with dexpanthenol for wound healing applications, Nanomaterials 10 (2020) 2469, https://doi.org/10.3390/nano10122469.
[72] C. Vilela, C. Moreirinha, E.M. Domingues, F.M.L. Figueiredo, A. Almeida, C.S. R. Freire, Antimicrobial and conductive nanocellulose-based films for active and intelligent food packaging, Nanomaterials 9 (2019) 980, https://doi.org/10.3390/nano9070980.
[73] C.C. Bastante, N.H.C.S. Silva, L.C. Cardoso, C.M. Serrano, E.J. Martínez de la Ossa, C.S.R. Freire, C. Vilela, Biobased films of nanocellulose and mango leaf extract for active food packaging: supercritical impregnation versus solvent casting, Food Hydrocoll. 117 (2021) 106709, https://doi.org/10.1016/j.foodhyd.2021.106709.
[74] W. Shao, S. Wang, J. Wu, M. Huang, H. Liu, H. Min, Synthesis and antimicrobial activity of copper nanoparticle loaded regenerated bacterial cellulose membranes, RSC Adv. 6 (2016) 65879–65884, https://doi.org/10.1039/C6RA07984A.
[75] H.O. Khalifa, H. Alkhoori, Beyond the glitter: gold nanoparticles as powerful weapons against multi-drug resistant pathogens, Front. Mol. Biosci. 12 (2025) 1612526, https://doi.org/10.3389/fmolb.2025.1612526.
[76] A. Jancik-Prochazkova, H. Michalkova, K. Cihalova, Z. Heger, M. Pumera, Microrobots for antibiotic-resistant Staphylococcus aureus skin colony eradication, ACS Appl. Mater. Interfaces 17 (2025) 39340–39348, https://doi.org/10.1021/acsami.5c08683.
[77] L.M. Tung, N.X. Cong, L.T. Huy, N.T. Lan, V.N. Phan, N.Q. Hoa, L.K. Vinh, N. V. Thinh, L.T. Tai, D.T. Ngo, K. Mølhave, T.Q. Huy, A.T. Le, Synthesis, characterizations of superparamagnetic $Fe_3O_4$-Ag hybrid nanoparticles and their application for highly effective bacteria inactivation, J. Nanosci. Nanotechnol. 16 (2016) 5902–5912, https://doi.org/10.1166/jnn.2016.11029.
[78] U. Strotmann, M.J. Durand, G. Thouand, C. Eberlein, H.J. Heipieper, S. Gartiser, U. Pagga, Microbiological toxicity tests using standardized ISO/OECD Methods—current state and outlook, Appl. Microbiol. Biotechnol. 108 (2024) 454, https://doi.org/10.1007/s00253-024-13286-0.
[79] M.D. Machado, E.V. Soares, Features of the microalga Raphidocelis subcapitata: physiology and applications, Appl. Microbiol. Biotechnol. 108 (2024) 219, https://doi.org/10.1007/s00253-024-13038-0.
[80] M.D.N. Ramos, C.S. Santana, C.C.V. Velloso, A.H.M. da Silva, F. Magalhães, A. Aguiar, A review on the treatment of textile industry effluents through fenton processes, Process Saf. Environ. Prot. 155 (2021) 366–386, https://doi.org/10.1016/j.psep.2021.09.029.
[81] E. Forgacs, T. Cserháti, G. Oros, Removal of synthetic dyes from wastewaters: a review, Environ. Int. 30 (2004) 953–971, https://doi.org/10.1016/J.ENVINT.2004.02.001.
[82] B. El Allaoui, H. Chakhtouna, N. Zari, H. Benzeid, A. el kacem Qaiss, R. Bouhfid, Process for cellulose-alginate core–shell microspheres fabrication and the influence of drying conditions on their structural and adsorption performances, Cellulose (2024), https://doi.org/10.1007/s10570-024-05954-1.
[83] H. Eskandarloo, A. Kierulf, A. Abbaspourrad, Nano- and micromotors for cleaning polluted waters: focused review on pollutant removal mechanisms, Nanoscale 9 (2017) 13850–13863, https://doi.org/10.1039/c7nr05494g.
[84] R. Merdoud, F. Aoudjit, L. Mouni, V.V. Ranade, Degradation of methyl orange using hydrodynamic cavitation, $H_2O_2$, and photo-catalysis with $TiO_2$-coated glass fibers: key operating parameters and synergistic effects, Ultrason. Sonochem. 103 (2024) 106772, https://doi.org/10.1016/j.ultsonch.2024.106772.
[85] L. Zhou, Y. Shao, J. Liu, Z. Ye, H. Zhang, J. Ma, Y. Jia, W. Gao, Y. Li, Preparation and characterization of magnetic porous carbon microspheres for removal of methylene blue by a heterogeneous fenton reaction, ACS Appl. Mater. Interfaces 6 (2014) 7275–7285, https://doi.org/10.1021/am500576p.